The coupling mechanism of mammalian respiratory complex I

One Sentence Summary: Conformational changes in the quinone binding site and formation of water wires in the E-channel initiate proton pumping by modulating pK_as of key residues.

Authors: Domen Kampjut[1] and Leonid A. Sazanov[1*]

Affiliations:

[1] IST Austria, Am Campus 1, 3400 Klosterneuburg, Austria

*Correspondence: sazanov@ist.ac.at

Abstract

Mitochondrial complex I couples NADH:ubiquinone oxidoreduction to proton pumping by an unknown mechanism. Here we present cryo-EM structures of ovine complex I in five different conditions, including turnover, at resolutions up to 2.3-2.5 Å. Resolved water molecules allowed us to experimentally define the proton translocation pathways. Quinone binds at three positions along the quinone cavity, as does the inhibitor rotenone that also binds within subunit ND4. Dramatic conformational changes around the quinone cavity couple the redox reaction to proton translocation during "open" to "closed" state transitions of the enzyme. In the induced deactive state, the "open" conformation is arrested by the ND6 subunit. We propose a detailed molecular coupling mechanism of complex I, which is an unexpected combination of conformational changes and electrostatic interactions.

Complex I is the largest of the respiratory complexes and in mammals is composed of 45 subunits with a total mass of about 1 MDa (Figure 1a). It catalyzes the transfer of two electrons from NADH to ubiquinone, coupled to the translocation of four protons across the bacterial or inner mitochondrial membrane, generating proton-motive force (*pmf*). It can also work in reverse, using *pmf* to reduce NAD^+ (*1*, *2*). Fourteen core subunits conserved in all species are necessary for the reaction. About 30 eukaryotic supernumerary subunits contribute to the regulation and stability, but are nevertheless crucial for the catalytic activity of the mammalian complex I (*1*, *3*). Initial crystal structures of bacterial enzyme (*4*, *5*) were followed by cryo-EM structures of mammalian mitochondrial complexes (*6–9*).

The catalytic mechanism of complex I, in particular the coupling between NADH:ubiquinone oxidoreduction and proton pumping over a distance of more than 200 Å, remains elusive. In the peripheral arm (PA) of the enzyme, electrons from NADH are accepted by FMN and passed along a chain of iron-sulfur clusters to cluster N2 and to ubiquinone, which binds in a narrow tunnel at the interface of the PA with the membrane domain (MD) (Figure 1a). MD comprises four separate proton pumps connected by a string of conserved charged residues along the middle of the entire MD length, forming the central hydrophilic axis. The closest to the quinone cavity is the E channel composed of ND1, ND6 and ND4L subunits, followed by three homologous antiporter-like subunits ND2, ND4 and ND5 (Figure 1a). Antiporters are composed of two symmetry-related half-channels of five trans-membrane helices (TMH) each, with N-terminal half thought to be open to the matrix and C-terminal half to the intermembrane space (IMS). Half-channels contain conserved key residues, lysine or glutamate, sitting on broken TMH7/TMH12 and are connected into a full channel by a central lysine from broken TMH8. The N-terminal key TMH7 lysine forms a pair with the conserved TMH5 glutamate, thought to modulate the pK_a of lysine (*1*, *4*, *5*).

The crucial energy-releasing step in the reaction is likely quinone reduction or its release out of the cavity because there is no drop in the mid-point redox potential of electron carriers until the electron reaches the final cluster N2 and quinol is released into bilayer (*10*, *11*). Molecular dynamics (MD) simulations suggested that diffusion of quinol out of the cavity is accompanied by the rearrangement of the quinone cavity loops (*12*). Quinol was also predicted to bind at two broad sites, one in the deep part of the cavity next to N2 (Q_d, or MD sites #1-2) and one in the shallow part (Q_s, or MD sites #4-5) close to the exit from the tunnel (*13*, *14*).

We proposed that the negative charge within the quinone cavity initiates conformational changes in the E-channel, propagating further into the antiporters via the

central hydrophilic axis, facilitated by flexible broken TM helices (*1*, *4*). These movements would influence interactions between the key lysine/glutamate residues within and between antiporters, leading to pK_a changes and proton translocation (*5*). In the alternative electrostatic spring proposal, coupling in the membrane domain is coordinated by a wave of electrostatic interactions (*15*). The most detailed mechanism includes quinol-induced changes of charge state of conserved residues, leading to forward and backward electrostatic waves, breaking and formation of water wires in the antiporters and proton pumping (*16*, *17*). However, all proposals so far lack experimental grounding and thus specifics of any conformational changes.

Complex I either isolated or within supercomplexes have so far been observed in two states, the closed and the open conformation which differ in the PA-MD angle (*6*, *7*, *9*) (Figure 1b). The opening coincides with unfolding of several loops, which can be divided into the quinone cavity forming loops and the interface forming loops (Figure 1c). The former include the 49 kDa β1-β2 loop (yellow) and the PSST loop (grey) that form the deep part of the quinone binding pocket and the ND1 TMH5-6 loop (green) that forms the shallow part of the pocket. The interface-forming loops consist of the ND3 TMH2-3 loop (orange) and the TMH3-4 loop of ND6 (blue). Closed-to-open transition is also associated with a notable rotation of the C-terminal half of ND6 TMH3 (blue) and the appearance of the π-bulge in the middle of the helix (*8*, *9*).

It has been argued that the open conformations of mouse and bovine complex I correspond to the deactive state, which is a catalytically inert state of complex I that occurs at elevated temperatures (30-37ºC) in the absence of substrates and can be reversed by slow turnover (*8*, *18*, *19*). However, open and closed conformations complex I were observed within active preparations of ovine respiratory supercomplexes (*9*, *20*), which suggest that the open conformation *per se* is not a deactive state but a *bona fide* catalytic intermediate of complex I.

To investigate the catalytic mechanism of complex I in detail, we compared high resolution cryo-EM structures of ovine complex I in five different conditions: native (no additions), NADH (enzyme reduced in the presence of NADH), rotenone (enzyme inhibited by rotenone in the presence of NADH), deactive (enzyme converted into deactive state) and turnover (enzyme flash-frozen while actively catalyzing NADH:decyl-ubiquinone oxidoreduction).

Comparison of open and closed conformations of complex I

An active and stable complex I preparation in a mild LMNG detergent enabled us to achieve resolutions of up to 2.3 Å for PA, 2.5 Å for MD and 2.6 Å overall, the highest for any

complex I study so far (Figure 1b, Figures S1-5). We built an almost complete model of complex I (96.9% residues modelled), with better defined geometry in previously ambiguous regions and including experimentally defined water molecules. We also resolved other high-resolution features, including post-translational modifications (Figures S6-7, Supplementary Text).

Our datasets contained a mixture of open and closed conformations of complex I arising from the combined side- and frontward tilting of the PA by up to 7º as described previously (*6*, *7*, *9*) (Figure S9d). The relative ratios between open and closed conformations were roughly the same in most datasets with the exception of the deactive, which completely lacked a closed conformation, and rotenone-inhibited, which had a smaller proportion of the closed state (Figure 1b).

In each dataset, several open classes could be classified. The most open classes (largest PA-MD angle) of the native, deactive and rotenone datasets showed partial disordering of the ND6 TMH4, 49 kDa N-terminus, anchor helix of ND5 and B14.7, which could represent a partially disassembled or deactivated enzyme. In other open classes these regions were ordered and did not differ from each other, particularly at the catalytically significant sites. The different degrees of openness in open classes thus likely reflect the loose PA-MD interface rather than functionally different states of complex I. We therefore treat open complex I as a single, albeit heterogeneous, state.

Opening of complex I coincided with disordering of several PA-MD interface forming loops (Figure 1c, S6c-e). In all of the datasets we observed disordering of the central part of the ND3 loop, the ND6 loop and the amphipathic helix (residues 259-272) of the supernumerary 39 kDa subunit. In the entire ND1 subunit, dramatic tilts of most helices resulted in up to 5 Å displacements at the matrix side, which propagate the conformational change all the way to the E-channel and also lead to the observed tilting of the PA (Figure S9d,e). Strikingly, as the ND1 TMH4 bends near Tyr142 upon such transition, this tyrosine swings out by almost 180º, freeing the space for the conserved Glu192 to move within hydrogen bonding distance of the conserved Glu143 (Figure 2a). Changes in the density appearance indicate that at least one of the glutamates becomes protonated in the open state, as the estimated pK_a increases by ~2 units for both (ProPKa software (*21*)). The formation of the π-bulge in ND6 TMH3, resulting in a remarkable 120º rotation of half of the helix, accompanies this closed to open transition (Figure 2b).

Quinone binding loops

In contrast to the interface forming loops, the conformations of the quinone site loops (49 kDa, PSST and ND1), depended not only on the openness, but also on the ligands bound and the redox state of the whole complex.

The 49 kDa loop was ordered in the retracted (out of quinone cavity) conformation in closed classes and disordered in the open classes of the native, turnover and deactive datasets. When rotenone was bound in the Q_d site in open complex I, this loop was ordered in the retracted conformation, suggesting that binding of a ligand in the Q_d site can order the loop. Notably, in open classes of NADH-reduced enzyme (but not closed classes), the 49 kDa loop was ordered in the novel extended (into the quinone cavity) conformation, shortening the cavity considerably (Figure 2d). Since the extended conformation was not observed in the rotenone and turnover datasets, which also contained NADH, the quinone-like ligand probably must be fully ejected from the cavity before the loop can extend.

ND1 loop was similarly ordered in the "down" conformation in the closed classes and disordered in the open classes. Only in NADH open classes (but not closed), however, ND1 loop rearranged into an "up" position, which displaced the ND3 loop as well as the other two ND1 matrix side loops (Figure 2e). Disordering of ND1 loop breaks several salt bridges, among which are highly conserved ND1_Glu214-PSST_Arg81 and ND1_Glu202-PSST_Arg77. Mutagenesis showed inhibitory effects of PSST_Arg77 and PSST_Arg81 mutations and MD simulations suggested that quinone can only diffuse within the cavity when the ND1 loop is disordered (*22*). In the "up" conformation, ND1_Glu214 formed an alternative salt bridge with ND1_Arg62, while ND1_Glu202 was exposed into the cavity (Figure 2e). ND1 loop did not switch into the "up" conformation in rotenone and turnover datasets, which also contained NADH, suggesting that binding of the ligand in the quinone cavity reverses the NADH-induced changes and could be an important step during the catalytic cycle.

The PSST loop itself also changed the conformation in most datasets. In the closed classes, it adopted the "raised" conformation, in which residues 48-51 bulge out into the quinone cavity, while in the open classes they form part of the β-sheet. Furthermore, residues 75-80 flip in the open classes, resulting in a 180º rotation of PSST_Arg77 (Figure 2c). Only in the rotenone dataset, however, the PSST loop always adopted the raised conformation and PSST_Arg77 contributed to rotenone binding.

Rotenone binds in three sites, including a unique site in the antiporter subunit.

Rotenone is one of the strongest specific inhibitors (IC_{50} ~ 1nM) of mammalian complex I (*23*). Because rotenone is much bulkier than typical Q-like inhibitors (such as piericidin A), it was hypothesized that it cannot penetrate into the Q cavity and might instead block it by binding outside (*24*). However, in the rotenone dataset, we observed rotenone density in the Q_d site in all 3D classes, coordinated by the key 49kDa_Tyr108 and 49kDa_His59, mimicking DQ and piericidin A binding in *T. thermophilus* (ROT1, Figure 3a-c) (*4*). Additionally, in the open classes, a second rotenone molecule was found in the Q_s site close to ND1_Arg25 (MD site #4 (*13*, *14*)) (ROT2, Figure 3a,d). Finally, in the open2 and open3 classes (84% of all particles), a third rotenone density was unexpectedly observed in the ND4 subunit, far away from the quinone cavity (ROT3, Figure 3a,e). This binding site is created by tilting out of the TMH6 and is deep between TMH5-7, directly contacting the key ND4_Lys206 in the proton channel (Figure 3f). The ND4 binding site could correspond to the lower affinity (80 nM) binding site reported for the deactive conformation (*23*), which would also be consistent with changes that we observe in the deactive conformation, exposing this pocket (Figure 3f). Binding in the ND4 site could also explain why rotenone has been observed to inhibit Na/H^+ antiporter activity of deactive complex I (*25*). ND4-bound rotenone, curiously, did not influence the conformations of the proton pumping residues, despite being bound by ND4_Lys206. It would be interesting to see if other inhibitors bind in this region, particularly biguanides which bind more strongly to the deactive enzyme (*19*). Inhibitors specific for antiporters could be a useful tool for studies on proton pumping.

As noted above, in the open enzyme binding of two rotenone molecules in the quinone cavity ordered the 49 kDa and PSST loops (Figure 3b) but not ND1 or ND3 loops, which suggests that ligand binding to the open complex I directly affects the conformations of the PSST and 49 kDa loops, while the ordering of the ND3 and ND1 loops can only happen upon reduction or closing of the complex. Overall, rotenone appears to be unique among complex I inhibitors by having multiple binding sites, which may explain its high affinity for the enzyme.

Deactivation leads to tilting of the ND6 TMH4 helix, arresting the complex

To better understand the structural rearrangements leading to complex I deactivation, we prepared deactive ovine complex I by incubation without substrates at an increased temperature (Figure S9a-c) (*26*) and collected a cryo-EM dataset. The deactive sample did not contain any closed conformation but we could classify four open classes, which were overall more open than the native open classes. They also had a large portion of the B14.7 subunit

disordered and classes 3 and 4 also showed some disorder around the horizontal helix HL and its TM anchor, the N-terminus of the 49 kDa subunit and the TMH5 of ND4 (Figure 3a,f).

The most striking feature of all deactive classes, however, was the almost complete relocation (by tilting) of the ND6 TMH4 helix, accompanied by the insertion of the TMH3-4 loop between the PA and MD, as well as unfolding of the 112-118 ND6 β-sheet (Figure 3g). TMH3-4 loop gets disordered in the open state and TMH3 acquires a π-bulge, which is likely the "waiting" state of the catalytic cycle when quinone cavity loops get partially and transiently disordered. During prolonged absence of turnover, unfolding proceeds to encompass wider regions of the complex further away from the quinone cavity and results in TMH4 tilt and a stable insertion of ND6 loop between the two arms, preventing transition into closed conformation and thus deactivating the enzyme. Reversal of this process is consequently slow and requires multiple turnovers. The stable decoupling of matrix and membrane arms of complex I and perhaps also the rearrangements within the ND4 subunit are consistent with the observation that deactive bovine complex I is a Na/H^+ antiporter (*25*).

A very distinct deactive state structure is a definite proof that open state of complex I is a part of catalytic cycle and not a deactive form as proposed earlier (*8*, *18*). Open enzyme is thus a quinone-binding, i.e. "waiting", intermediate. The high kinetic barrier of active-to-deactive transition in mammals is thus explained by the large-scale reorganization of ND6. This is consistent with previous mouse and bovine "deactive" conformations which showed weak ND6 TMH4 density, indicating that they were partly, but not fully deactivated (or the fully deactive state class was not separated in 3D classification) (*8*, *18*). They are also consistent with *Y. lipolytica* structures in which ND6 TMH4 is much less likely to shift due to its close association with ND5 TMH16 and NUJM (homologue of B14.7) subunit (*27*). Hence, *Y. lipolytica* complex I quasi-deactive state is actually a waiting open state, in which the ND3 loop is disordered and so is susceptible to alkylation, but the enzyme reverts into the processive state without lag.

Under turnover quinone binds both in the deep and shallow sites

We collected a dataset of complex I incubated with NADH and decylubiquinone and flash-frozen before the substrates were exhausted. Under such active turnover conditions, one may expect to identify quinone binding modes and any conformational changes associated with the catalytic cycle, provided that relevant conformations can be separated by classification and that the enzyme explores the entire conformational space in the absence of membrane and *pmf*.

Such an approach with *Y. lipolytica* enzyme suggested an absence of large conformational changes, although medium resolution (4.5 Å) prevented further mechanistic insights (*28*).

Both open and closed classes of our turnover dataset contained a clear density for bound NADH, showing that this is the most populated state of the NADH-binding site during turnover, even though Fe-S clusters and FMN are likely to be mostly reduced since quinol release is a limiting step (*11*, *29*).

Closed complex I contained two bound decylubiquinones. Quinone in the deep binding pocket (Q_d) was bound between 49kDa_His59 and 49kDa_Tyr108, exactly where rotenone binds (Figure 4a). We also observed a strong density near the entry to the quinone cavity, overlapping with the second rotenone site and the MD site #4, which we modelled as another molecule of decylubiquinone (Figure 4a,c). Notably, residues 49kDa_Asp160 and 49kDa_His59, which coordinate quinone in the Q_d site had a continuous density between them, indicating the existence of a salt bridge, probably as a result of proton donation to quinone (Figure 4d). This density was not present in any of the other conditions (Figure 4e, S10h) and 49kDa_Asp160 density was weak as is usual for unbound carboxylates in cryo-EM (*30*). Therefore, it is likely that 49kDa_His59 first donates a proton to reduce quinone and then accepts a proton from 49kDa_Asp160, so that negative charge resides on 49kDa_Asp160 and the salt bridge is formed. This is the first experimental demonstration that 49kDa_His59/Asp160 pair act as a proton donor for the quinone. It also indicates that the species bound in the Q_d site in the turnover dataset is quinol rather than quinone.

In the open turnover classes, a quinone density was present only in the shallow pocket (Q_s) but it was located further outwards compared to the closed class and was overlapping with the MD site #5 (Figure 4b,c). The mobile loops of the quinone binding cavity were disordered to approximately the same extent as in the native open classes and we did not see any density in the deep binding pocket. This suggests that enzyme opening affects quinone binding and dynamics in the cavity and likely facilitates quinol ejection or quinone uptake by the complex. Presence of two molecules of quinone in the closed class is probably an artefact of using decylubiquinone with its short carbon tail. If native ubiquinone-10 were bound in Q_d, its isoprenoid tail would clearly prevent quinone binding in Q_s in the tight quinone cavity of the closed enzyme (Figure 4f). Opening of complex I widens the negatively charged quinone binding cavity, in a large part due to PSST re-arrangements (Figure 4f), which will facilitate quinone movements in and out of cavity before and after reduction. In the NADH open conformation, the cavity becomes much shorter, mostly due to 49 kDa loop insertion, which will facilitate quinol ejection.

The role of water molecules in quinone protonation and proton pumping

Abundant water molecules that we observed in the PA cryoEM density were mostly consistent across the different conditions; hence they are likely to represent tightly bound stationary molecules (Figure S10c). Several of them are close to the iron-sulfur clusters, but none lie directly between them, thus they are not likely to participate in electron tunneling as proposed before from simulations (*31*). Uniquely from other FeS clusters, N2 contains two water molecules at hydrogen bonding distance, which may help to elevate its redox potential (Figure S10d).

High resolution of the turnover data allowed us to analyze the mechanistically important water distribution in the MD. At 2.5 Å resolution in cryo-EM, most water molecules are resolved, as confirmed by our analyses – we observed significantly more waters (1293) in the open class MD at 2.5 Å than predicted by Dowser software (742). The MD was less hydrated than the PA, with a clear pattern of hydrated matrix / IMS surfaces and abundantly hydrated central axis with relatively dry regions in between (Figure 5a). About 90 waters were identified on the central axis, within 6 Å from key residues, while only about 60 waters were predicted by Dowser, indicating that we likely have a complete experimental picture of water distribution in the MD core. Especially hydrated were the cavities around key TMH7 and TMH12 lysines/glutamate, containing about 10 waters each. A similar overall pattern was obtained for the turnover closed state MD, although fewer waters were identified (Figure S10b) due to lower resolution (2.9 Å).

All the key protonatable residues along the entire hydrophilic axis from the ND5 tip to the Q cavity are clearly interconnected via many water molecules, with the exception of a long break in the E channel between ND4L_Glu34 and ND3_Asp66 in the open state (green arrow in Figure 5a). This is caused by the ND6 TMH3 π-bulge with bulky hydrophobic residues such as Phe68 and Met64 blocking the path. Strikingly, when TMH3 rotates and the π-bulge disappears in the closed state, these residues are rotated away and are replaced by the conserved glycines 62-63, creating a water-filled cavity between ND3_Asp66 and ND4L_Glu34. This creates a water chain extending from ND1 all the way to ND2 only in the closed state (Figure 5b,c). TMH3 of ND6 is the most conserved TM helix in the MD, and even conservative mutations in the π-bulge area are highly detrimental to activity (*5*), indicating that breaking and reforming of the water wire is probably essential for the mechanism. Furthermore, three critical glutamates of the E channel, ND1_Glu143, ND4L_Glu34 and ND4L_Glu70 become charged

in the closed enzyme as suggested by their density appearance and pattern of hydrogen bond interactions (Figure S9i). ND4L_Glu34 also rotates away from ND4L_Glu70 as they become charged and surrounded by waters.

Beyond the E-channel we did not observe any conformational changes in any dataset, including turnover, neither in the broken antiporter helices nor in the traverse HL helix or connecting β-hairpins. HL helix thus probably serves mainly a structural role and is not involved in the coupling mechanism as advocated previously (*4*, *5*, *16*, *17*). Analysis of the proton transfer pathways connecting Grotthuss-competent residues (Lys, Glu, Asp, His, Tyr, Thr, Ser) and experimentally identified waters within hydrogen bonding distances (with bond slack up to ~4 Å) suggested that E-channel and ND2 and ND4 antiporters lack any connections to the IMS (Figure 5a, with dashed pathways). These parts of the structure are particularly dry and hydrophobic. The matrix-facing part of ND4 is less dry and can allow connection to matrix via conserved ND4_His220 upon conformational changes in broken TMH7, where ND4_His220 sits. This histidine is not conserved in ND2, which lacks any clear connections to the matrix. Notably, the distal antiporter ND5 is radically different – the key TMH12 Lys392 is clearly connected to the IMS via the conserved ND5_Asp393 and many waters around. Connection to the matrix side via the conserved ND5_His248 also exists. The side chain of this histidine is roughly in the same position as ND4_His220, but it sits on TMH8, replacing LysTMH8 in ND5. Thus, both ND4_His220 and ND5_His248 sit on broken helices, allowing for their flexibility as needed to control the connectivity to the matrix, in tandem with key LysTMH8 in ND4 and the additional conserved essential Lys336 in ND5. The breaks of about 6 Å prevent links of ND4_His220 to the matrix and ND5_His248 to the IMS (Figure 5a, red color dashes), consistent with out-of-sync operation of ND4 and ND5 (below) and probably preventing back-leak of protons.

The observed high connectivity along the central axis, the lack of links to the IMS side in antiporters other than ND5 and the absence of any conformational changes in antiporters even under turnover lead us to propose that all four protons may be pumped out to IMS via ND5. This is a radical departure from the traditional view that protons are ejected one by one by each antiporter individually, as originally proposed by us (*4*, *5*). However, the clear experimental facts above argue that this new ND5-only model should be considered as a more likely option. All four protons could hop over to ND5 via the abundant central axis links using conserved connecting histidines (cyan in Figure 5d) as a temporary storage. The ND5 subunit, despite being distal, is clearly the most conserved of antiporters and has unique features

supporting this proposal (Supplementary Text). The input of protons from the matrix clearly happens in ND5 and possibly also ND4, with ND2 / E-channel inputs less likely. In all scenarios, protons taken up from the matrix are probably quickly re-distributed along the fully inter-connected central axis (Figure 5a).

Proton pumping mechanism

Absence of conformational changes in antiporter-like subunits under turnover suggests that proton pumping in them is mainly electrostatically driven. This is supported by a clear pattern of changes in charge distribution of key residues between open and closed states revealed by the analysis of cryo-EM densities for hydrogen bonds and carboxylate side-chains (Figure S9f-i, Table S7). There is an asymmetric distribution of charges between the antiporters, with ND4 being out of sync with ND2 and ND5 (Figure 5d). This may help to prevent excessive electrostatic imbalance in the MD if all antiporters were to transfer charges in sync. Asymmetry is probably achieved by the replacement of the key TMH12 lysine with glutamate (E378) in ND4. The switch in the orientation/openness of the proton channels is likely associated with the global change in the structure, i.e. between open and closed states. Since the open state is energetically more favorable, it is likely that in this relaxed state most channels are open to the matrix side, so that protein can re-protonate the central axis from the matrix.

We propose the following proton pumping mechanism. Our results indicate that quinone can bind and enter the cavity only in the open state of the complex. The proton pumping cycle is initiated by quinone binding, accompanied by the transition to the closed state with the ND1 and 49 kDa loops reordering into the “down” and “retracted” conformations, allowing quinone movement into the deep site, where it gets reduced. These changes lead to ND6 TMH3 rotation (Supplementary Movie 1), which in turn creates a water wire (isolated from bulk solvent) linking the Q cavity to ND4L_Glu34/Glu70 (Figure 5c). These residues donate two protons for re-protonation of the quinol-coordinating residues 49kDa_Asp160/His59/Tyr108, which creates a strong negative charge in ND4L. This charge is compensated by the nearby ND2_GluTMH5 taking up the proton from its partner LysTMH7. Absence of positive charge on LysTMH7 removes electrostatic barrier and allows the connecting LysTMH8 to lose a proton to LysTMH12. This positive charge is compensated by the nearby ND4_GluTMH5, donating proton to ND4_LysTMH7. The connecting ND4_LysTMH8 is protonated from the matrix, but the positive charge on LysTMH7 prevents the movement of its proton further on to GluTMH12. This glutamate loses proton to the IMS

357 due to electrostatic interactions with charged LysTMH7 and LysTMH8, and its negative charge
358 is compensated by ND5_GluTMH5 taking up the proton from ND5_LysTMH7, similarly to
359 the situation at ND4L/ND2 interface. As in ND2, this leads to protonation of ND5_LysTMH12
360 by Lys336 (or His248), completing a transition from open to closed state.
361 Subsequent diffusion of quinol towards the shallow site causes disordering of the 49
362 kDa, ND1 and ND3 loops as well as re-formation of the π-bulge and the opening of the
363 complex. As enzyme gets reduced, the 49 kDa loop gets extended and the ND1 loop flips
364 upwards, helping to eject the quinol (Supplementary Movie 2). Upon complex I opening
365 ND4L_Glu34/E70 will be re-protonated, via ND2 and the central axis, as the water wire to the
366 Q site will be now broken. At this stage one proton is likely to be ejected from the E channel
367 into IMS. Arrival of protons to ND4L_Glu34/Glu70 will cause the nearby ND2_GluTMH5 to
368 donate a proton to LysTMH7. As the connecting LysTMH8 is protonated from the matrix, this
369 additional positive charge will help to drive the LysTMH12 proton into IMS. As positive
370 charge on ND2_LysTMH12 is lost, its neighbor ND4_GluTMH5 acquires the proton back
371 from LysTMH7. Loss of charge on LysTMH7 allows the connecting LysTMH8 to lose its
372 proton to GluTMH12, and due to electrostatic interactions the nearby ND5_GluTMH5 will
373 lose its proton to LysTMH7. As in ND2, the connecting ND5 residue is protonated from the
374 matrix and the double positive charge on it and LysTMH7 will drive LysMTH12 proton out,
375 re-setting the system to the open state. Thus, simple electrostatic interactions are sufficient to
376 drive proton translocation in a consistent manner across each antiporter, a feature which is
377 allowed by out-of-sync operation of ND4.
378 In our scenario the N-terminal Glu-Lys pairs serve mainly as polar/charge switches,
379 controlling proton translocation between TMH8 and TMH12 residues. A similar proposal was
380 put forward before on the basis of MD simulations, with a key role for opening/closing of Glu-
381 Lys pairs (*17*). We do not observe such opening/closing on a predicted scale, but rather a
382 change in charge state. Proton transfer within these pairs, as suggested by our observations
383 (Figure S9f-i) is probably a more robust way to achieve consistent switching of channels.
384 Furthermore, instead of forward and reverse electrostatic waves (*16*), proton translocation in
385 our mechanism proceeds via two forward electrostatic waves driven by protonation and de-
386 protonation of ND4L glutamates, in turn driven by quinone oxidoreduction via defined
387 conformational changes in ND1/E-channel. Our mechanism is applicable both to traditional
388 one-per-antiporter or new ND5-only modes of pumping, as the only difference in the case of

the ND5-only model would be a re-distribution of protons towards the ND5 subunit (instead of directly into IMS) via the central axis.

Concluding remarks

On the basis of the above model of proton pumping and the various, many of them novel, conformations of complex I observed here, we propose a first detailed model of the entire catalytic cycle (Supplementary Text and Figure S11). Our mechanism explains the directionality and tight coupling of the reaction, as (1) NADH-induced changes in the quinone cavity can only happen in the open conformation of the complex, (2) reduction of quinone happens only in the closed state and (3) proton pumping is induced during the transitions between the two states. The mechanism is easily reversible: high *pmf* would promote the reverse reaction by driving charge transitions in antiporters in reverse to those in Figure 5d. Translocation of protons into the matrix would lead to transfer of protons from the 49kDa_Tyr108/His59/Asp160 triad to ND4L glutamates, creating a negative charge on the triad. It would promote quinol binding and oxidation, as well as lower the N2 redox potential, enabling reverse electron transfer from N2 to FMN and NAD^+.

The key novel features of our mechanism are: firstly, the delivery of negative charge from the redox reaction site towards antiporters via defined concerted conformational changes propagating from the Q site towards the E channel; secondly, the description of how this negative charge drives the proton pumping in the antiporters via electrostatic wave propagation; and, thirdly, the optional, but probable, alternative pathway of proton ejection into IMS only via the ND5 subunit. Although we cannot exclude that additional intricacies might be revealed by studies of complex I in energized liposomes or using a time-resolved cryo-EM approach, the mixed conformational-electrostatic model proposed is strongly supported by our data, is fully consistent with available mutagenesis data and is sufficient to explain the previously enigmatic mechanism.

Materials and Methods

Purification of complex I

Purification procedures were done at 4°C as described before (*20*). Briefly, mitochondria were purified from fresh ovine heart tissue as described before and stored as pellets at -80 degrees. The sheep hearts were cooled on ice within an hour of slaughter, while transport and mitochondrial isolation took additional ~10 hours. On the day of complex I purification, a 10 g aliquot of mitochondrial pellet was thawed and inner mitochondrial membranes were isolated by rupturing mitochondria by homogenization in 100 mL Milli-Q water, addition of KCl to 150 mM and centrifugation at 50000 g for 45 min. Afterwards, membranes were resuspended in 100 mL of buffer M (20 mM HEPES, pH 7.4, 40 mM NaCl, 1 mM EDTA, 10% v/v glycerol, 2 mM DTT and 0.002% PMSF), centrifuged again and resuspended in 50 mL of buffer M. To solubilize the membrane proteins, 10% lauryl maltose neopentyl glycol (LMNG) was added dropwise to 1% final concentration to the membrane suspension and stirred for 45 minutes. Upon centrifugation (50000g, 45 min) the supernatant was filtered with a 0.22 μm filter and loaded onto a 45 mL Q-sepharose HP anion exchange column equilibrated in buffer Q-A (20 mM HEPES pH7.4, 40 mM NaCl, 2 mM EDTA, 10% v/v glycerol, 1 mM DTT, 0.05% LMNG). The column was washed with 75mL Q-A buffer, 50mL of 10% Q-B buffer (Q-A with 1 M NaCl), 125 mL of 20% Q-B buffer and finally complex I was eluted by a 200 mL linear gradient with 20-27% Q-B buffer. Complex I-containing fractions were pooled, concentrated to ~15 mg/mL using a Millipore 100-kDa cut-off filter and stored, with 30% glycerol added, under liquid nitrogen. A 250 μL sample was thawed on ice when cryoEM grids were prepared, loaded onto a Superose 6 10/300 gel filtration column equilibrated in buffer GF (20 mM HEPES, pH 7.4, 50 mM NaCl, 1 mM EDTA, 0.002% LMNG) to remove excess detergent and remaining protein contaminants. The purest and the most concentrated fractions of complex I eluted at ~11.5 mL and were concentrated to 3.5 mg/mL and used immediately for cryo-EM grid preparation. Deactive complex I was prepared by incubating a concentrated aliquot of complex I after anion exchange at 32ºC for 30 min. To prevent delipidation and proteolysis, 0.5 mg/mL of 1:4 mixture of cardiolipin and dioleoylphosphatidylcholine and 0.0075% PMSF were added to the sample. Afterwards, the sample was cooled on ice and injected to the gel filtration column as described above.

Electron cryo-microscopy

CHAPS was added (final concentration 0.2%) to the protein sample before grid preparation to improve ice quality and particle distribution. The native and the deactive complex I samples were frozen without further substrate additions. For the NADH dataset 5 mM NADH was added to the protein 20 min before the grid preparation and the samples were incubated on ice. For the rotenone dataset, NADH (5 mM) was added to complex I sample, incubated for 1 min on ice and followed by the addition of 300 μM rotenone (dissolved in DMSO, final DMSO concentration in the sample ~1%) and 20 min incubation on ice. For the turnover dataset, a mixture of substrates and CHAPS was prepared at 2x working concentration (2 mM DQ, 2 mM NADH and 0.4% CHAPS) and mixed in 1:1 ratio with 6 mg/mL complex I immediately before applying to the grid, blotting and freezing. With this simple procedure, complex I was active for 20 s before being frozen and less than 10% of substrates would have been consumed in this time. Final concentration of complex I used for grid preparation was 3 mg/mL for all samples.

2.7 μL protein sample was applied to a freshly glow-discharged (0.7 mbar and 30 mA for 2 min in the ELMO Glow Discharge unit, Agar Scientific, Stansted, UK) Quantifoil 0.6/1 copper grid and blotted using the Whatman filter paper No1 for 6-8 s using a blotting force of 25 at 4°C and 100% humidity in an FEI Vitrobot Mark IV. Grids were flash-frozen in liquid ethane and stored in liquid nitrogen until data-collection.

Native, NADH, rotenone and turnover grids were imaged using a 300 kV Titan Krios electron microscope equipped with a Falcon III camera operating in an integrating mode at Cryo-Electron Microscopy and Tomography Core Facility in CEITEC, Brno. Turnover, NADH and rotenone datasets were imaged at a nominal magnification of 130000x with a physical pixel size of 1.061 Å. Total electron exposure of 89 e/Å^2 was fractionated into 40 frames of 21 ms each. Native dataset was imaged at a nominal magnification of 165000x with a physical pixel size 0.83 Å. Total electron exposure of 98 e/Å^2 was fractionated into 40 frames of 25 ms each. Images were collected from 3x3 patches of holes using image shift – resulting beam tilt error was small and refined during processing and this mode of acquisition allowed for a high speed of collection. Deactive complex I was imaged in using a 300 kV Titan Krios electron microscope equipped with a K3 camera operating in a super-resolution mode at the Institute of Science and Technology Austria. Grids were imaged at a nominal magnification of 81000x and physical pixel size of 1.055 Å. Total electron exposure of 78.5 e/Å^2 was fractionated into 50 frames of 88 ms each. The deactive dataset was collected using SerialEM

with an active beam tilt compensation, hence beam tilt error was not refined separately for each of the nine holes imaged using the image shift method (*32*).

Image processing

We started with 2284 movies for the native dataset, 1443 movies for NADH dataset, 4239 movies for the turnover dataset, 2323 movies for the rotenone dataset and 2065 movies for the deactive dataset. The micrographs were included in the further processing steps if the Thon rings extended to 4 Å (turnover dataset) or 5 Å (all other datasets) according to the CTFFIND maximum resolution estimate. Processing was done in RELION 3.0 and 3.1 (*33*) unless otherwise stated. Movie frames were aligned using MotionCor2 (*34*) and initial CTF parameters were estimated from averaged images using CTFFIND 4.1.13 (*35*). Autopicking with 2D class averages as references was done in RELION and resulted in 295630 particles for the native dataset, 364499 particles for NADH dataset, 938197 particles for the turnover dataset, 354690 particles for the rotenone dataset and 740026 particles for the deactive dataset.

For the sake of consistency, processing steps were done as similarly as possible for all the datasets. Particles were extracted at 3x the physical pixel size and processed using one round of 2D classification and one round of 3D classification (Figures S1-5). Good classes were then extracted at full pixel size and autorefined into a single "consensus" structure. CTF parameters and per-particle trajectories were then refined in an iterative manner (one round of CTF refinement followed by Bayesian polishing and another CTF refinement). This led to a consensus refined complex I structure of all particles, reaching nominally high resolutions (up to 2.5Å in turnover dataset) but with blurring around the edges and some weaker subunits (42 kDa and B14.7) suggesting a large degree of conformational heterogeneity and presence of partially disassembled particles. Particles were therefore 3D classified without searches to remove damaged particles and then focus-reverse-classified to sort out the heterogeneity as done earlier (*9*). Briefly, all the intact particles were focus-refined using a peripheral arm mask and then classified without searches using a loose membrane mask to finely classify states with slightly different angles between the two arms. This procedure resulted in a single closed class and 3-4 open classes from each dataset, based on which atomic models were built, analyzed and compared. In most datasets, finer sub-classification of classes with different masks, in particular around the quinone binding cavity, was tried but did not result in finding additional conformational states of complex I. Further classifications of consensus refinements of MD or PA of all particles also did not result in finding additional conformational classes. Although

515 some datasets have shown preferential orientation of particles, this did not influence the quality
516 of final maps due to the presence of sufficient amounts of particles in other orientations.
517 In the native dataset, the first round of 3D classification was done with k = 6 classes
518 and regularization parameter T = 6, which resulted in 148307 good particles. Upon duplicates
519 removal, consensus refinement and two rounds of CTF refinement and Bayesian polishing,
520 128964 particles were refined around the matrix arm and subjected to final classification
521 without searches around the membrane arm with k = 6 and T = 20. This resulted in four good
522 classes with 91979 particles in total and two partially broken classes. The good classes were
523 refined and post-processed separately to give final maps for model building.
524 In the NADH dataset, the first round of 3D classification was done with k = 6 and T=4,
525 which resulted in 276169 good particles. After duplicates removal, consensus refinement, two
526 rounds of CTF parameter refinement and Bayesian polishing, another 3D classification with k
527 = 6 and T=8 without searches was performed to remove damaged particles. Remaining 182053
528 particles were refined around the PA and subjected to classification around the membrane arm
529 with k = 6 and T = 8. This resulted in 4 good classes with a total of 140630 particles and two
530 classes with bad density and partially disassembled complex. Particles from the four good
531 classes were refined, post-processed and the maps were used for model building.
532 In the deactive dataset, the first round of 3D classification was done with k = 6 and T
533 = 4 and resulted in 458556 good particles. After a consensus refinement, another 3D
534 classification step without searches and with k = 6 and T = 10 was performed to remove further
535 damaged particles. This resulted in 272990 particles, which were refined around the PA and
536 classified around the membrane arm using 3D classification without searches and k = 4 and T
537 = 10. This resulted in four classes that differed from each other by the degree of openness.
538 They were subjected to two rounds of CTF parameter refinement, Bayesian polishing,
539 refinement and post-processing to obtain the final density maps used for model building.
540 In the rotenone dataset, the first round of 3D classification was done with k = 6 and T
541 = 4 and resulted in 175658 good particles after duplicate removal. After two rounds of CTF
542 parameter refinement, Bayesian polishing and auto-refinement, another 3D classification
543 without searches and with k = 6 and T = 8 was performed to remove broken particles, which
544 resulted in 142565 good particles, which were focus-refined around the membrane domain.
545 Because of the low abundance of the closed class in this dataset, the closed class was separated
546 by 3D classification around the membrane arm with k = 6 and T = 10. The rest of the particles
547 were 3D classified separately with k = 6 and T = 6 to better separate different open classes.
548 The resulting particles were refined, post-processed and used for model building.

In the turnover dataset, the initial 3D classification was done with k = 6 and T = 4 and resulted in 518117 good particles after duplicated removal. After two rounds of CTF parameter refinement, Bayesian polishing and auto-refinement, another 3D classification without searches and k = 6 and T = 8 was performed to remove damaged particles, resulting in 344541 good particles retained. These were then 3D classified around the membrane arm without searches and with k = 6 and T = 8. Four of the resulting classes contained good particles with a total of 257669 particles, which were refined and post-processed for model building. The density within the quinone cavity of the closed class appeared broken, hence this class was further classified without searches and with k = 3 and T = 50. This resulted in one major class with about 55% particles that had better defined density in the quinone cavity and elsewhere and another minor class with about 30% of particles that had worse density overall but otherwise no significant differences to the major class. Only the major closed class was used for model building. For Closed MD model, all the particles of the turnover closed class were focus-refined around the MD, however.

Model building and refinement

The models presented in this paper are based on the initial 3.9 Å structure of ovine complex I determined previously (PDB 5LNK) (*6*). Membrane domain and peripheral arm were built on the basis of 2.5 Å and 2.3 Å focus-refinements of all the open particles from the turnover dataset which allowed us to improve the geometry, fit and completeness of the models significantly (Supplementary Text). We were also able to model additional lipid molecules, as well as several known post-translational modifications, including N-terminal acylations of subunits B18, B14.5b and B14.7, N-formyl methionines in ND6, ND5 and ND4L, symmetric dimethylation of 49 kDa Arg85 and phosphorylation of 42 kDa Ser36 (*36*) (Figure S7). For accurate modelling of water molecules, particularly to avoid false positives, we filtered the maps by local resolution and resampled them at 0.5 Å per pixel in Relion. After this procedure, water molecules displayed strong signal (> 2 σ), had nearly spherical densities, were not clashing with other atoms and participated in hydrogen bonds, which are all strongly indicative of real water molecules. This allowed automatic placement of water molecules in COOT, which were then all checked and corrected manually, to leave only waters with clear density and fulfilling geometry criteria. Using this procedure, we could reliably place water molecules not only into 2.3-2.8 Å structures but also into the closed MD focus refined map (overall resolution 2.9 Å, higher in the core). The two highest resolution open PA and open MD models

were then rigid-body fit into all the classes, corrected in *Coot* (*37*) and refined using *PHENIX* software (*38*). We used two rounds of a single cycle of group ADP refinement followed by three cycles of global minimization in real space (with secondary structure, Ramachandran and c-beta restrains enabled) to optimize B-factors so that electron radiation-damaged carboxylate side-chains acquire high B-factors and do not lead to main-chain distortions as described previously (*9*). To maintain consistency, we performed this procedure first with rotamer fit option enabled, checked and corrected the model in *Coot* and then finally repeated the procedure without rotamer fit.

Structure analysis and preparation of figures

Geometry and density fit of the models was analyzed using MolProbity and EMRinger (*39*, *40*). pK_a was estimated using PROPKA 3.1 software (*21*). Visualization and analysis of the models and corresponding density maps was done in PyMOL 2.2.3 and UCSF Chimera. The highest resolution maps from PA and MD focused refinements were approaching Nyquist resolution and were resampled at 0.5 Å pixel size in RELION for depiction purposes, which resulted in a smoother density (Figures S6-7).

Activity measurements

Complex I NADH:DQ oxidoreduction activity was measured at 30°C spectrophotometrically by following the NADH ($\varepsilon = 6.1\ mM^{-1}\ cm^{-1}$) oxidation at 340 nm using a Shimadzu UV-2600 UV-VIS spectrophotometer. Reaction buffer was optimized for the ovine CxI purified in LMNG before (20 mM HEPES, pH 7.4, 50 mM NaCl, 1 mM EDTA, 0.2% CHAPS, 0.05% LMNG, 0.25 mg/mL DOPC:CL lipids, 3.5 mg/mL bovine serum albumin, 200 μM NADH and 200 μM DQ) (*20*). Complex I was incubated in the above buffer with stirring for 5 min before the measurement was started by NADH addition. Labelling with NEM was performed by incubating a sample of 1 mg/mL of purified complex I with 1 mM NEM on ice for 5 min, after which NEM was neutralized by the addition of 1 mM DTT. Submitochondrial particles were prepared by resuspending 1 g of mitochondrial pellet in 8 mL of 10 mM HEPES, pH 7.0 and 250 mM sucrose, frozen at -80 degrees and thawed again. Mitochondria were then pelleted in a bench-top centrifuge, washed with 4 mL of the same buffer and resuspended in a total of 4 mL of the above buffer with 10 mM $MgSO_4$ added. Mitochondria were then sonicated on ice (10 15 s bursts at 30 W), centrifuged (27100 g, 20 min) to remove remaining mitochondria and the submitochondrial particles were finally collected by ultracentrifugation (82000 g, 30 min)

615 and resuspended in 2 mL of the sucrose buffer. NADH:DQ oxidoreduction activity of SMPs
616 was measured in the same buffer as for isolated complex I but without lipids and detergents
617 and with additional 10 μM CCCP.
618

References and Notes

1. L. A. Sazanov, A giant molecular proton pump: Structure and mechanism of respiratory complex I. *Nat. Rev. Mol. Cell Biol.* **16**, 375–388 (2015).
2. J. Hirst, Mitochondrial Complex I. *Annu. Rev. Biochem.* **82**, 551–575 (2013).
3. D. A. Stroud, E. E. Surgenor, L. E. Formosa, B. Reljic, A. E. Frazier, M. G. Dibley, L. D. Osellame, T. Stait, T. H. Beilharz, D. R. Thorburn, A. Salim, M. T. Ryan, Accessory subunits are integral for assembly and function of human mitochondrial complex I. *Nature*. **538**, 123–126 (2016).
4. R. Baradaran, J. M. Berrisford, G. S. Minhas, L. A. Sazanov, Crystal structure of the entire respiratory complex I. *Nature*. **494**, 443–448 (2013).
5. R. G. Efremov, L. A. Sazanov, Structure of the membrane domain of respiratory complex i. *Nature*. **476**, 414–421 (2011).
6. K. Fiedorczuk, J. A. Letts, G. Degliesposti, K. Kaszuba, M. Skehel, L. A. Sazanov, Atomic structure of the entire mammalian mitochondrial complex I. *Nature*. **538**, 406–410 (2016).
7. J. Zhu, K. R. Vinothkumar, J. Hirst, Structure of mammalian respiratory complex I. *Nature*. **536**, 354–358 (2016).
8. A. N. A. Agip, J. N. Blaza, H. R. Bridges, C. Viscomi, S. Rawson, S. P. Muench, J. Hirst, Cryo-em structures of complex i from mouse heart mitochondria in two biochemically defined states. *Nat. Struct. Mol. Biol.* **25**, 548–556 (2018).
9. J. A. Letts, K. Fiedorczuk, G. Degliesposti, M. Skehel, L. A. Sazanov, Structures of Respiratory Supercomplex I+III2 Reveal Functional and Conformational Crosstalk. *Mol. Cell*. **75**, 1131-1146.e6 (2019).
10. L. Euro, D. A. Bloch, M. Wikström, M. I. Verkhovsky, M. Verkhovskaya, Electrostatic interactions between FeS clusters in NADH:Ubiquinone oxidoreductase (complex I) from Escherichia coli. *Biochemistry*. **47**, 3185–3193 (2008).
11. M. Wikström, V. Sharma, V. R. I. Kaila, J. P. Hosler, G. Hummer, New perspectives on proton pumping in cellular respiration. *Chem. Rev.* **115**, 2196–2221 (2015).
12. V. Sharma, G. Belevich, A. P. Gamiz-Hernandez, T. Róg, I. Vattulainen, M. L. Verkhovskaya, M. Wikström, G. Hummer, V. R. I. Kaila, Redox-induced activation of the proton pump in the respiratory complex i. *Proc. Natl. Acad. Sci. U. S. A.* **112**, 11571–11576 (2015).
13. J. Warnau, V. Sharma, A. P. Gamiz-Hernandez, A. Di Luca, O. Haapanen, I. Vattulainen, M. Wikström, G. Hummer, V. R. I. Kaila, Redox-coupled quinone dynamics in the respiratory complex I. *Proc. Natl. Acad. Sci. U. S. A.* **115**, E8413–E8420 (2018).
14. O. Haapanen, A. Djurabekova, V. Sharma, Role of Second Quinone Binding Site in Proton Pumping by Respiratory Complex I. *Front. Chem.* **7**, 221 (2019).
15. M. Verkhovskaya, D. A. Bloch, Energy-converting respiratory Complex I: On the way to the molecular mechanism of the proton pump. *Int. J. Biochem. Cell Biol.* **45**, 491–511 (2013).
16. V. R. I. Kaila, Long-range proton-coupled electron transfer in biological energy conversion: Towards mechanistic understanding of respiratory complex i. *J. R. Soc. Interface*. **15**, 20170916 (2018).

17. A. Di Luca, A. P. Gamiz-Hernandez, V. R. I. Kaila, Symmetry-related proton transfer pathways in respiratory complex I. *Proc. Natl. Acad. Sci. U. S. A.* **114**, E6314–E6321 (2017).

18. J. N. Blaza, K. R. Vinothkumar, J. Hirst, Structure of the Deactive State of Mammalian Respiratory Complex I. *Structure*. **26**, 312-319.e3 (2018).

19. S. Matsuzaki, K. M. Humphries, Selective inhibition of deactivated mitochondrial complex i by biguanides. *Biochemistry*. **54**, 2011–2021 (2015).

20. J. A. Letts, G. Degliesposti, K. Fiedorczuk, M. Skehel, L. A. Sazanov, Purification of ovine respiratory complex i results in a highly active and stable preparation. *J. Biol. Chem.* **291**, 24657–24675 (2016).

21. M. H. M. Olsson, C. R. SØndergaard, M. Rostkowski, J. H. Jensen, PROPKA3: Consistent treatment of internal and surface residues in empirical p K a predictions. *J. Chem. Theory Comput.* **7**, 525–537 (2011).

22. E. Galemou Yoga, O. Haapanen, I. Wittig, K. Siegmund, V. Sharma, V. Zickermann, Mutations in a conserved loop in the PSST subunit of respiratory complex I affect ubiquinone binding and dynamics. *Biochim. Biophys. Acta - Bioenerg.* **1860**, 573–581 (2019).

23. V. G. Grivennikova, E. O. Maklashina, E. V Gavrikova, A. D. Vinogradov, Interaction of the mitochondrial NADH-ubiquinone reductase with rotenone as related to the enzyme active/inactive transition. *Biochim. Biophys. Acta - Bioenerg.* **1319**, 223–232 (1997).

24. O. Haapanen, V. Sharma, A modeling and simulation perspective on the mechanism and function of respiratory complex I. *Biochim. Biophys. Acta - Bioenerg.* **1859** (2018), pp. 510–523.

25. P. G. Roberts, J. Hirst, The deactive form of respiratory complex I from mammalian mitochondria is a Na+/H+ antiporter. *J. Biol. Chem.* **287**, 34743–51 (2012).

26. A. B. Kotlyar, A. D. Vinogradov, Slow active/inactive transition of the mitochondrial NADH-ubiquinone reductase. *BBA - Bioenerg.* **1019**, 151–158 (1990).

27. A. K. Parey, O. Haapanen, V. Sharma, H. Köfeler, T. Züllig, S. Prinz, K. Siegmund, I. Wittig, D. J. Mills, J. Vonck, W. Kuhlbrandt, V. Zickermann, High-resolution cryo-EM structures of respiratory complex I - mechanism , assembly and disease. *Sci. Adv.* **5**, 1–47 (2019).

28. K. Parey, U. Brandt, H. Xie, D. J. Mills, K. Siegmund, J. Vonck, W. Kühlbrandt, V. Zickermann, Cryo-EM structure of respiratory complex I at work. *Elife*. **7**, e39213 (2018).

29. A. D. Vinogradov, V. G. Grivennikova, The Mitochondrial Complex I: Progress in Understanding of Catalytic Properties. *IUBMB Life (International Union Biochem. Mol. Biol. Life)*. **52**, 129–134 (2001).

30. J. Wang, On the appearance of carboxylates in electrostatic potential maps. *Protein Sci.* **26**, 396–402 (2017).

31. T. Hayashi, A. A. Stuchebrukhov, Electron tunneling in respiratory complex i. *J. Phys. Chem. B*. **115**, 5354–5364 (2011).

32. M. Schorb, I. Haberbosch, W. J. H. Hagen, Y. Schwab, D. N. Mastronarde, Software tools for automated transmission electron microscopy. *Nat. Methods*. **16**, 471–477

(2019).

33. J. Zivanov, T. Nakane, B. O. Forsberg, D. Kimanius, W. J. Hagen, E. Lindahl, S. H. Scheres, New tools for automated high-resolution cryo-EM structure determination in RELION-3. *Elife*. **7**, e42166 (2018).

34. S. Q. Zheng, E. Palovcak, J.-P. Armache, K. A. Verba, Y. Cheng, D. A. Agard, MotionCor2: anisotropic correction of beam-induced motion for improved cryo-electron microscopy. *Nat. Methods*. **14**, 331–332 (2017).

35. A. Rohou, N. Grigorieff, CTFFIND4: Fast and accurate defocus estimation from electron micrographs. *J. Struct. Biol.* **192**, 216–221 (2015).

36. J. Carroll, I. M. Fearnley, J. E. Walker, Definition of the mitochondrial proteome by measurement of molecular masses of membrane proteins. *Proc. Natl. Acad. Sci. U. S. A.* **103**, 16170–16175 (2006).

37. P. Emsley, B. Lohkamp, W. G. Scott, K. Cowtan, Features and development of Coot. *Acta Crystallogr. D. Biol. Crystallogr.* **66**, 486–501 (2010).

38. P. D. Adams, P. V. Afonine, G. Bunkóczi, V. B. Chen, I. W. Davis, N. Echols, J. J. Headd, L.-W. Hung, G. J. Kapral, R. W. Grosse-Kunstleve, A. J. McCoy, N. W. Moriarty, R. Oeffner, R. J. Read, D. C. Richardson, J. S. Richardson, T. C. Terwilliger, P. H. Zwart, IUCr, *PHENIX* : a comprehensive Python-based system for macromolecular structure solution. *Acta Crystallogr. Sect. D Biol. Crystallogr.* **66**, 213–221 (2010).

39. B. A. Barad, N. Echols, R. Y. R. Wang, Y. Cheng, F. Dimaio, P. D. Adams, J. S. Fraser, EMRinger: Side chain-directed model and map validation for 3D cryo-electron microscopy. *Nat. Methods*. **12**, 943–946 (2015).

40. V. B. Chen, W. B. Arendall, J. J. Headd, D. A. Keedy, R. M. Immormino, G. J. Kapral, L. W. Murray, J. S. Richardson, D. C. Richardson, MolProbity: all-atom structure validation for macromolecular crystallography. *Acta Crystallogr. D. Biol. Crystallogr.* **66**, 12–21 (2010).

41. H. Zheng, M. Chruszcz, P. Lasota, L. Lebioda, W. Minor, Data mining of metal ion environments present in protein structures. *J. Inorg. Biochem.* **102**, 1765–1776 (2008).

42. J. M. Berrisford, L. A. Sazanov, Structural Basis for the Mechanism of Respiratory Complex I. *J. Biol. Chem.* **284**, 29773–29783 (2009).

43. M. Schulte, K. Frick, E. Gnandt, S. Jurkovic, S. Burschel, R. Labatzke, K. Aierstock, D. Fiegen, D. Wohlwend, S. Gerhardt, O. Einsle, T. Friedrich, A mechanism to prevent production of reactive oxygen species by Escherichia coli respiratory complex I. *Nat. Commun.* **10**, 2551 (2019).

44. M. Murai, H. Miyoshi, Current topics on inhibitors of respiratory complex i. *Biochim. Biophys. Acta - Bioenerg.* **1857**, 884–891 (2016).

45. F. G. P. Earley, S. D. Patel, C. I. Ragan, G. Attardi, Photolabelling of a mitochondrially encoded subunit of NADH dehydrogenase with [3 H]dihydrorotenone. *FEBS Lett.* **219**, 108–112 (1987).

46. S. Uno, T. Masuya, K. Shinzawa-Itoh, J. Lasham, O. Haapanen, T. Shiba, D. Inaoka, V. Sharma, M. Murai, H. Miyoshi, *J. Biol. Chem.*, in press, doi:10.1074/jbc.RA119.012347.

47. A. Galkin, B. Meyer, I. Wittig, M. Karas, H. Schägger, A. Vinogradov, U. Brandt,

Identification of the mitochondrial ND3 subunit as a structural component involved in the active/deactive enzyme transition of respiratory complex I. *J. Biol. Chem.* **283**, 20907–20913 (2008).

48. O. Haapanen, V. Sharma, Role of water and protein dynamics in proton pumping by respiratory complex I. *Sci. Rep.* **7** (2017), doi:10.1038/s41598-017-07930-1.

49. V. R. I. Kaila, M. Wikström, G. Hummer, Electrostatics, hydration, and proton transfer dynamics in the membrane domain of respiratory complex i. *Proc. Natl. Acad. Sci. U. S. A.* **111**, 6988–6993 (2014).

50. X. C. Zhang, B. Li, Towards understanding the mechanisms of proton pumps in Complex-I of the respiratory chain. *Biophys. Reports*. **5**, 219–234 (2019).

51. M. Sato, P. K. Sinha, J. Torres-Bacete, A. Matsuno-Yagi, T. Yagi, Energy transducing roles of antiporter-like subunits in Escherichia coli NDH-1 with main focus on subunit NuoN (ND2). *J. Biol. Chem.* **288**, 24705–24716 (2013).

52. E. Nakamaru-Ogiso, M. C. Kao, H. Chen, S. C. Sinha, T. Yagi, T. Ohnishi, The membrane subunit NuoL(ND5) is involved in the indirect proton pumping mechanism of Escherichia coli complex I. *J. Biol. Chem.* **285**, 39070–39078 (2010).

53. S. Dröse, S. Krack, L. Sokolova, K. Zwicker, H. D. Barth, N. Morgner, H. Heide, M. Steger, E. Nübel, V. Zickermann, S. Kerscher, B. Brutschy, M. Radermacher, U. Brandt, Functional dissection of the proton pumping modules of mitochondrial complex I. *PLoS Biol.* **9** (2011).

54. G. Belevich, J. Knuuti, M. I. Verkhovsky, M. Wikström, M. Verkhovskaya, Probing the mechanistic role of the long α-helix in subunit L of respiratory Complex I from Escherichia coli by site-directed mutagenesis. *Mol. Microbiol.* **82**, 1086–1095 (2011).

55. S. Steimle, C. Bajzath, K. Dörner, M. Schulte, V. Bothe, T. Friedrich, Role of Subunit NuoL for Proton Translocation by Respiratory Complex i. *Biochemistry*. **50**, 3386–3393 (2011).

56. P. J. Holt, D. J. Morgan, L. A. Sazanov, The Location of NuoL and NuoM Subunits in the Membrane Domain of the Escherichia coli Complex I: Implications for the mechanism of proton pumping. *J. Biol. Chem.* **278**, 43114–43120 (2003).

57. N. Battchikova, M. Eisenhut, E. M. Aro, Cyanobacterial NDH-1 complexes: Novel insights and remaining puzzles. *Biochim. Biophys. Acta - Bioenerg.* **1807**, 935–944 (2011).

58. J. M. Schuller, P. Saura, J. Thiemann, S. K. Schuller, A. P. Gamiz-Hernandez, G. Kurisu, M. M. Nowaczyk, V. R. I. Kaila, Redox-coupled proton pumping drives carbon concentration in the photosynthetic complex I. *Nat. Commun.* **11** (2020), doi:10.1038/s41467-020-14347-4.

59. M. E. Muehlbauer, P. Saura, F. Nuber, A. Di Luca, T. Friedrich, V. R. I. Kaila, *J. Am. Chem. Soc.*, in press, doi:10.1021/jacs.0c02789.

Acknowledgements

We thank Dr J. Novacek (CEITEC Brno) and Dr V.-V. Hodirnau (IST Austria) for their help with collecting cryo-EM datasets. We thank the IST Life Science and Electron Microscopy Facilities for providing equipment.

Funding: This work has been supported by iNEXT, project number 653706, funded by the Horizon 2020 programme of the European Union. This article reflects only the author's view and the European Commission is not responsible for any use that may be made of the information it contains. CIISB research infrastructure project LM2015043 funded by MEYS CR is gratefully acknowledged for the financial support of the measurements at the CF Cryo-electron Microscopy and Tomography CEITEC MU. This project has received funding from the European Union's Horizon 2020 research and innovation programme under the Marie Skłodowska-Curie Grant Agreement No. 665385.

Author contributions: DK purified complex I, performed biochemical assays, prepared cryo-EM grids, acquired and processed EM data, built and analyzed the atomic models and wrote the initial draft of the manuscript. LAS designed and supervised the project, acquired funding, analyzed data and revised the manuscript.

Competing interests: The authors declare no competing financial interests.

Data and materials availability: Atomic models resulting from this study were deposited in the PDB under the following accession codes: 6ZKO (native closed), 6ZKP (native open1), 6ZKQ (native open2), 6ZKR (native open3), 6ZKG (NADH closed), 6ZKH (NADH open1), 6ZKI (NADH open2), 6ZKJ (NADH open3), 6ZKS (deactive open1), 6ZKT (deactive open2), 6ZKU (deactive open3), 6ZKV (deactive open4), 6ZKK (rotenone closed), 6ZKL (rotenone open1), 6ZKM (rotenone open2), 6ZKN (rotenone open3), 6ZKC (turnover closed), 6ZKD (turnover open1), 6ZKE (turnover open2), 6ZKF (turnover open3), 6ZK9 (turnover PA-open), 6ZKA (turnover MD-open), 6ZKB (turnover MD-closed).

Cryo-EM maps used to generate these models were deposited in the EMDB: EMD-11256 (native closed), EMD-11257 (native open1), EMD-11258 (native open2), EMD-11259 (native open3), EMD-11248 (NADH closed), EMD-11249 (NADH open1), EMD-11250 (NADH open2), EMD-11251 (NADH open3), EMD-11260 (deactive open1), EMD-11261 (deactive open2), EMD-11262 (deactive open3), EMD-11263 (deactive open4), EMD-11252 (rotenone closed), EMD-11253 (rotenone open1), EMD-11254 (rotenone open2), EMD-11255 (rotenone open3), EMD-11244 (turnover closed), EMD-11245 (turnover open1), EMD-11246 (turnover

open2), EMD-11247 (turnover open3), EMD-11241 (turnover PA-open), EMD-11242 (turnover MD-open), EMD-11243 (turnover MD-closed).

Supplementary Materials

Supplementary Text

Supplementary Figures S1-S11

Supplementary Tables S1-S7

Supplementary Movies S1-S2

Main Figure Legends

Figure 1. Complex I catalyzes redox-coupled proton pumping. a. Core subunits necessary for the reaction of complex I are labelled with corresponding colors and mammalian supernumerary subunits are shown in grey. NADH and quinone binding sites are indicated. Membrane arm contains four separate proton pumping channels, three in the antiporter-like subunits ND2, ND4, ND5 and one in the E-channel composed of subunits ND1, ND6 and ND4L. **b.** Ovine complex I exists in open and closed conformations, the ratios of which differ between different conditions investigated. Resolution achieved for each state overall and for PA- or MD-focused refinements is shown. **c.** Conformational dynamics of the quinone binding site loops. Loops at the interface between the peripheral and membrane arms, ND3 (orange) and ND6 (blue) adopt different states shown schematically. Quinone binding cavity loops include the 49 kDa loop (yellow), PSST loop (grey) and ND1 loop (green), which also undergo radical changes. Residue numbers indicate start-end of loops. The eight iron-sulfur clusters that transfer electrons from NADH to quinone are shown as orange-yellow spheres.

Figure 2. Opening and reduction of the complex induce long-range conformational changes. a. Reogranization of the ND1 subunit upon opening with a detailed view of the rearrangements of the conserved glutamates which are part of the E-channel. On the left, open state is gray and closed state is colored by subunit, while on the right, open state is cyan and closed is green. **b.** TMH3 of ND6 rotates by almost 180º in the open state (cyan), acquires a π-bulge near Tyr60 and the TMH3-4 loop gets disordered. **c.** PSST loops and Arg77 undergo large conformational changes between open (cyan) and closed (green) states. **d.** 49 kDa loop is ordered in the closed state (green), gets disordered upon opening (cyan) and reorders in the extended position the reduced open state (pink). **e.** ND1 loop which is in the "down" conformation in the closed state (green), gets disordered upon opening and switched to the "up" conformation in the reduced open state (pink). In the "up" position, ND1 clashes with the ND3 (orange) and 49 kDa (yellow) loops, which are also reordered. Reorganization of the ND1 loop results in breaking of two salt bridges with PSST_Arg77 and Arg81 (grey).

Figure 3. Deactivation and rotenone inhibition elicit alternative conformations of complex I. a. The most open classes of rotenone-inhibited and deactive complex I exhibit disorder in the ND5 horizontal and anchor helix as well as in the B14.7 subunit (colored). TMH4 of ND6, which undergoes rearrangements in deactive state is labelled in pink. The three

rotenone binding sites are indicated as well; ROT2 binds to open classes only and ROT3 binds to open2 and open3 classes. **b.** PSST and 49 kDa loops do not change between open (cyan) and closed (green) rotenone states. Native open conformation is shown in grey. **c.** The deep rotenone binding site: rotenone is within hydrogen binding distance to 49kDa_His59 and Tyr108 and mimics the conformation of bound quinone during reduction from the N2 cluster. Rotenone density is shown at the contour of 2 σ (**c, e**) or 3 σ (**d**). **d.** The shallow rotenone binding site: rotenone is stabilized by polar interactions with conserved arginines and stacking interactions with ND1_Phe224. **e.** ND4 rotenone binding site: rotenone is stabilized by positively charged residues, including proton-pumping Lys206, Arg142 and by stacking interactions with Trp216. **f.** To open the ND4 subunit binding site, the outer TMH6 needs to undergo a slight tilting and rearrangement observed in rotenone open2 and open3 classes (cyan), but also in the most open class of the deactive dataset (orange). Native structure is overlaid in green. **g.** In deactive complex I ND6 TMH4 gets tilted (density in blue) towards the matrix-membrane arm interface and the TMH3-4 loop inserts between the two arms, stabilizing them in the open conformation.

Figure 4. Quinone density is observed at different binding sites in open and closed complex I during turnover. a. In closed complex I, one quinone molecule is bound in the deep pocket between 49kDa_Tyr108 and His59 and another in the shallow pocket close to ND1_Arg25. Density is shown at the σ contour of 1.3 (**a**), 2 (**b**), 1.8 (**d**) and 2 (**e**). **b.** In open complex I, a single quinone is bound at the entry to the quinone binding cavity close to ND1_Phe224. **c.** Comparison of binding positions of quinone and rotenone in different classes. **d.** Detailed view on the binding of quinone next to the N2 cluster and the density showing the salt bridge between 49kDa_His59 and Asp160. **e.** 49kDa_Asp160 displays weak density and no connection to His59 in all of the classes apart from closed turnover class; rotenone open2 structure shown here. **f.** Cross sections through the quinone binding cavity in closed, open and NADH-open states colored by electrostatic potential reveal that opening and reduction result in large changes of the quinone binding cavity shape. In closed state UQ_{10} is modelled (gray), based on decyl-ubiquinone binding and illustrating tight fit of the native substrate.

Figure 5. Quinone protonation and proton pumping requires coordinated water molecules. a. Central hydrophilic axis connects the three antiporters in the open state of complex I. Both N- and C-terminal Lys/Glu are abundantly hydrated. Water wires towards IMS

and matrix side are visible only in ND5. E-channel has a dry region between ND3_Asp66 and ND4L_Glu34 and no connection to IMS or matrix side. It is connected to the quinone binding cavity only in the closed state (green arrow), allowing for protons from ND4L_Glu34 and Glu70 to be delivered to Q-site (red arrow). **b.** Top view of the E-channel in open state of complex I shows that the E-channel dry region is caused by the ND6 π-bulge formation and ND4L_Glu34 rotation. **c.** Continuous water wire in the E-channel of the closed state of complex I. **d.** Proposed proton pumping mechanism. Charge distribution of the proton pumping residues differs between the open and the closed states. Colored circles correspond to glutamate/aspartate (red), lysine (blue) or histidine (cyan) and are shown in the same orientation as in Figure 1c. Full circles represent charged residues and empty circles are neutral (state of histidines is not clear). Arrows show proton movements to achieve the charge distribution as depicted in each state.

Online media files

Supplementary movie 1. Opening and closing of complex I result in large scale reorganization of ND1 and ND6 subunits.

Supplementary movie 2. Quinone diffusion out of the cavity is aided by conformational changes of the 49 kDa, ND1 and PSST loops during opening and reduction of the complex.

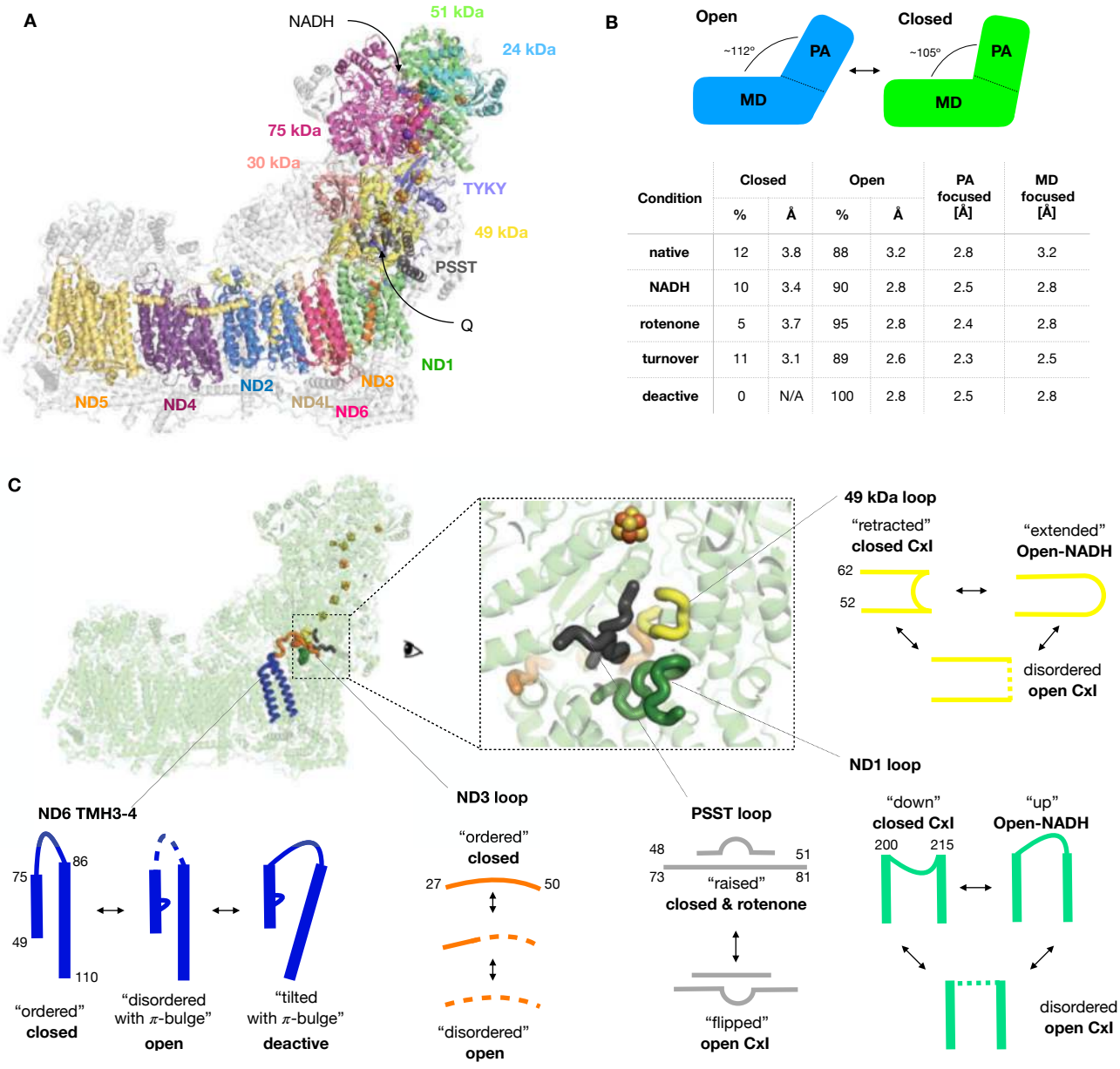

Condition	Closed		Open		PA focused [Å]	MD focused [Å]
	%	Å	%	Å		
native	12	3.8	88	3.2	2.8	3.2
NADH	10	3.4	90	2.8	2.5	2.8
rotenone	5	3.7	95	2.8	2.4	2.8
turnover	11	3.1	89	2.6	2.3	2.5
deactive	0	N/A	100	2.8	2.5	2.8

Figure 1

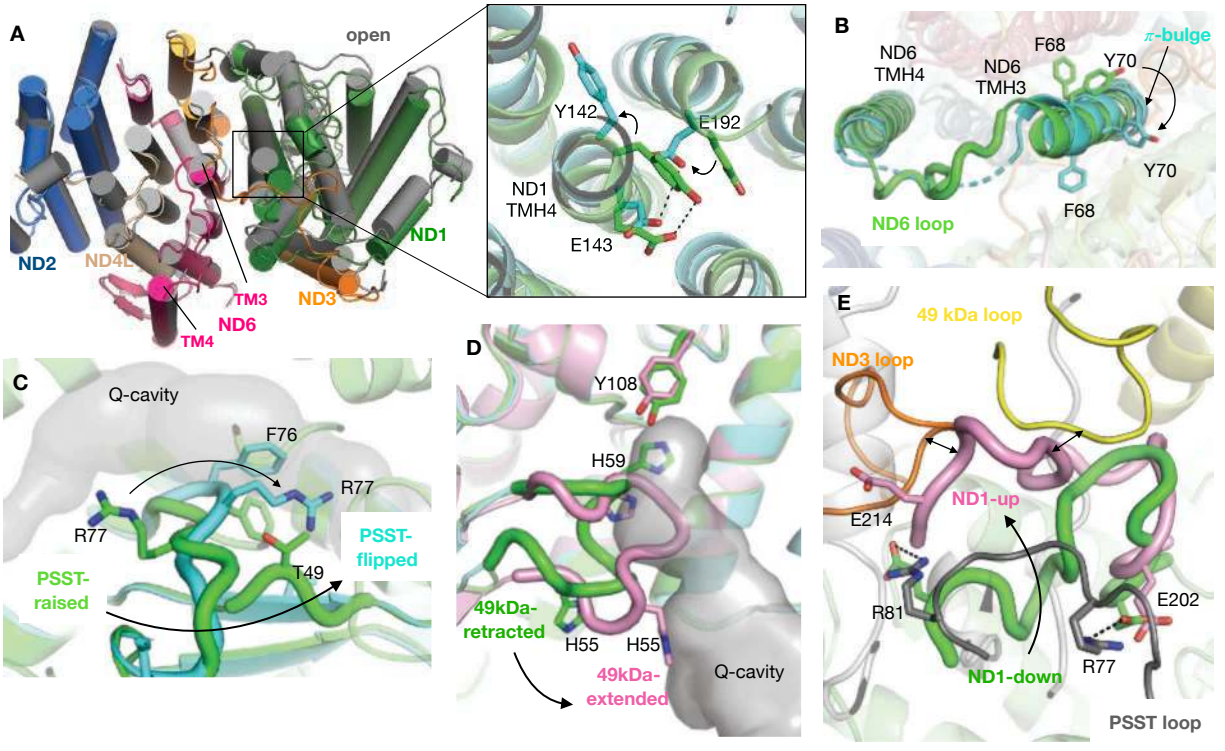
A
open
ND2
ND4L
TM3
ND3
ND1
TM4
ND6
Y142
E192
ND1
TMH4
E143
B
ND6
TMH4
ND6
TMH3
F68
Y70
π-bulge
Y70
F68
ND6 loop
C
Q-cavity
F76
R77
R77
PSST-
flipped
PSST-
raised
T49
D
Y108
H59
49kDa-
retracted
H55
H55
49kDa-
extended
Q-cavity
E
49 kDa loop
ND3 loop
ND1-up
E214
R81
E202
ND1-down
R77
PSST loop

Figure 2

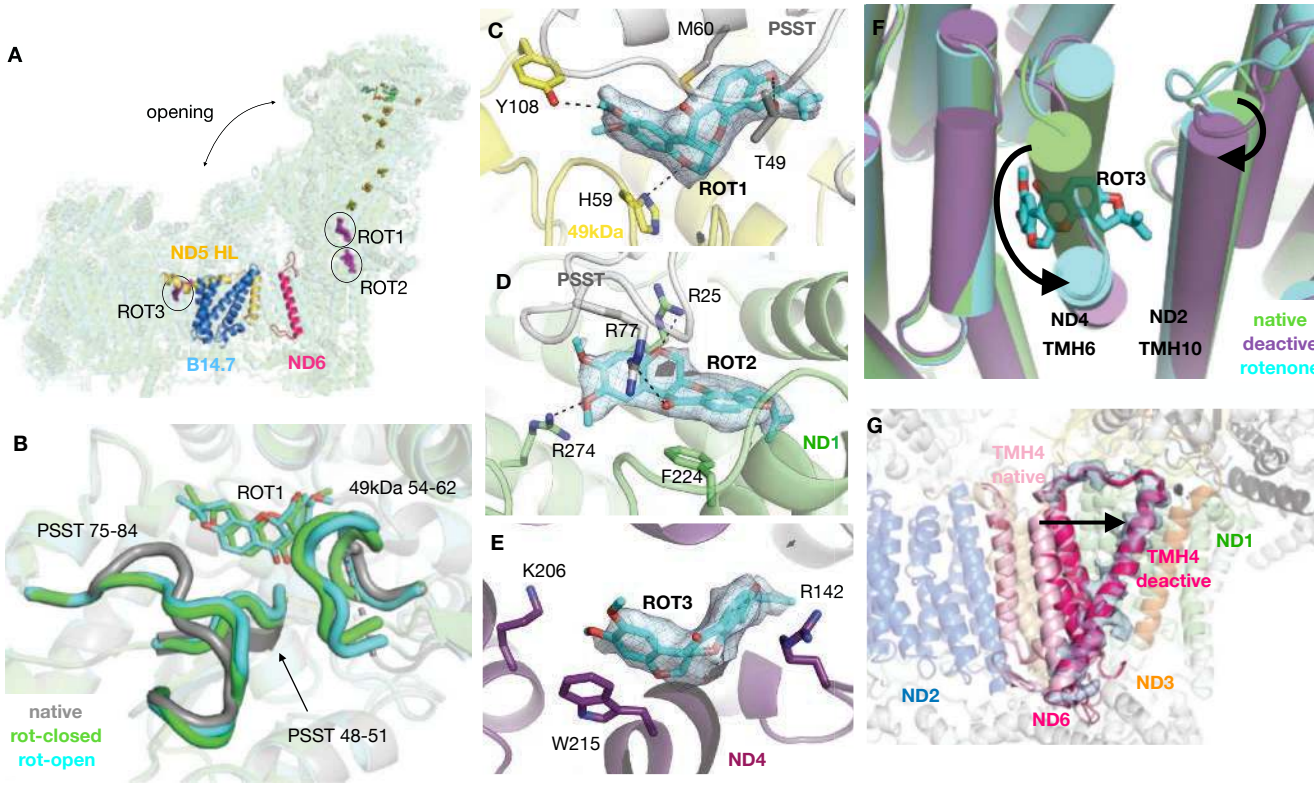
A
opening
ROT1
ROT2
ND5 HL
ROT3
B14.7
ND6
B
ROT1
49kDa 54-62
PSST 75-84
native
rot-closed
rot-open
PSST 48-51
C
M60
PSST
Y108
T49
H59
ROT1
49kDa
D
PSST
R25
R77
ROT2
ND1
R274
F224
E
K206
ROT3
R142
W215
ND4
F
ROT3
ND4
TMH6
ND2
TMH10
native
deactive
rotenone
G
TMH4
native
ND1
TMH4
deactive
ND3
ND2
ND6

Figure 3

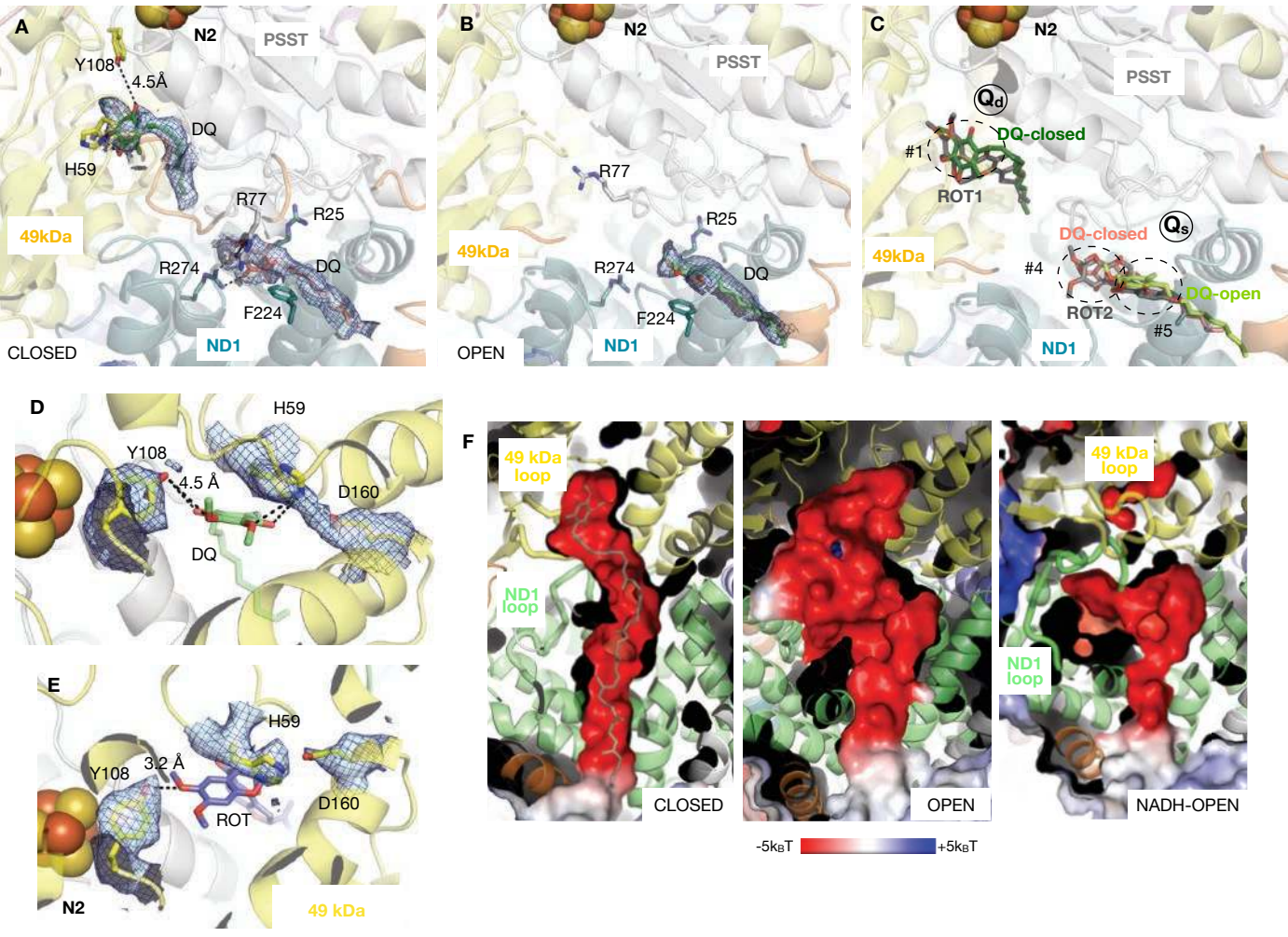
A
N2
PSST
Y108
4.5Å
DQ
H59
R77
R25
49kDa
R274
DQ
F224
ND1
CLOSED
B
N2
PSST
R77
R25
49kDa
R274
DQ
F224
ND1
OPEN
C
N2
PSST
Qd
DQ-closed
#1
ROT1
49kDa
DQ-closed
Qs
#4
DQ-open
ROT2
#5
ND1
D
H59
Y108
4.5 Å
D160
DQ
E
H59
Y108
3.2 Å
D160
ROT
N2
49 kDa
F
49 kDa loop
ND1 loop
CLOSED
OPEN
49 kDa loop
ND1 loop
NADH-OPEN
-5kBT
+5kBT

Figure 4

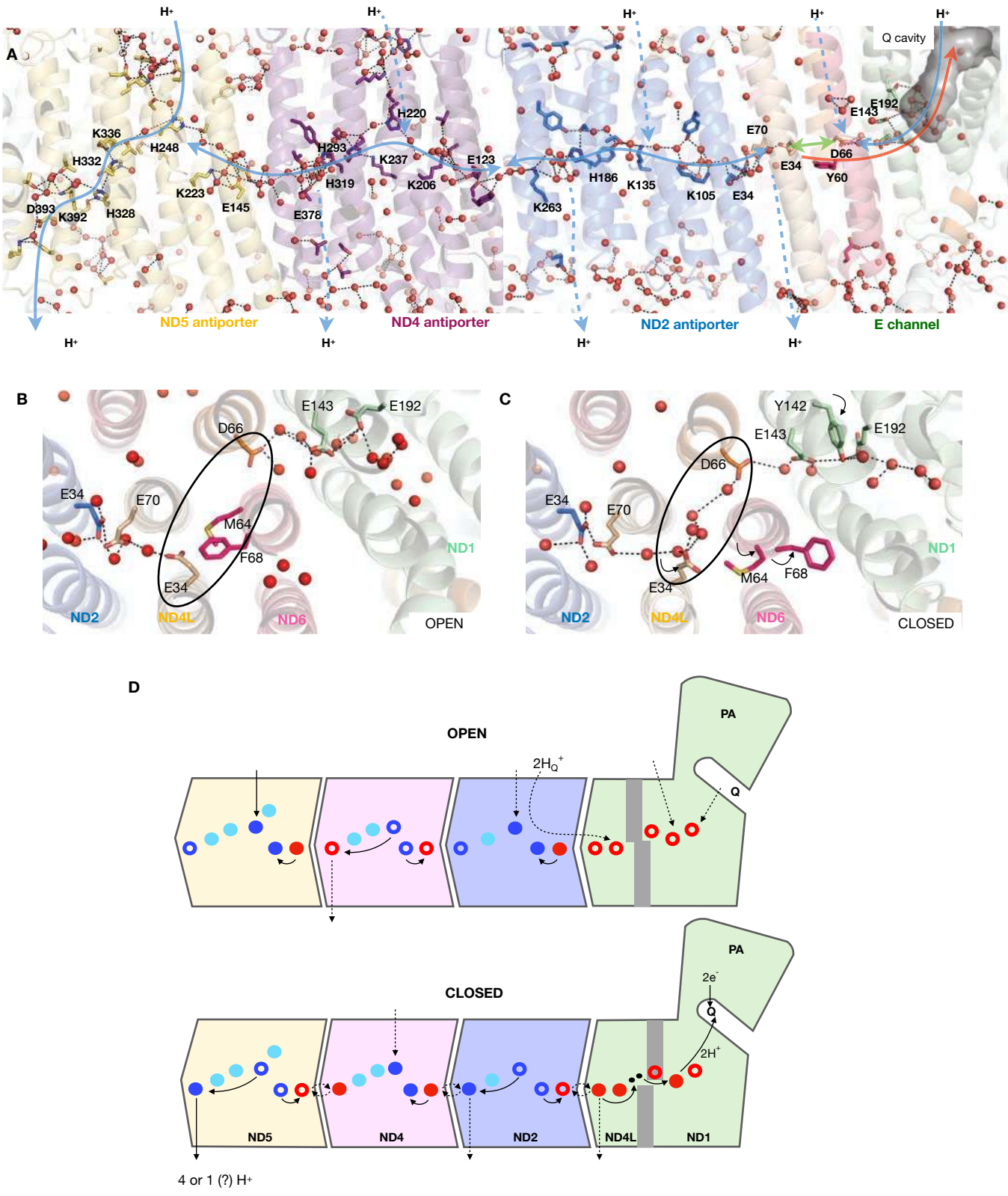
A
H+
Q cavity
K336
H248
H332
H293
H220
K237
E123
H319
K206
K223
E145
E378
D393
K392
H328
H186
K135
K263
K105
E34
E70
E143
E192
D66
Y60
ND5 antiporter
ND4 antiporter
ND2 antiporter
E channel
B
E143
E192
D66
E34
E70
M64
F68
E34
ND1
ND2
ND4L
ND6
OPEN
C
Y142
E143
E192
D66
E34
E70
E34
M64
F68
ND1
ND2
ND4L
ND6
CLOSED
D
OPEN
PA
2H$_Q^+$
Q
CLOSED
PA
2e$^-$
Q
2H$^+$
ND5
ND4
ND2
ND4L
ND1
4 or 1 (?) H+

Figure 5

Supplementary Text

High-resolution features of complex I

We modelled more and better-defined lipid molecules than previously, including cardiolipins and several lipid molecules bound above the quinone entry site, indicating the local distortion of the membrane plane around the quinone entry site. This puts the quinone entry site roughly between the two lipid leaflets and was proposed earlier to facilitate quinone flipping and diffusion (Figure S8a-d) (*28*). Cardiolipin, known to be essential for respiratory enzymes activity, is found in 8 locations (Figure S8a), some of them consistent with locations in other species (*8*, *18*) along with 5 new ones. Supernumerary subunit B14.7 is almost fully separated from the MD by a lipid cushion, hence this subunit could have been acquired solely for the interaction with complex III in the respiratory supercomplexes.

Furthermore, we observed density for several post-translational modifications, including N-terminal acylation of three of the supernumerary subunits, N-formyl methionine of three core subunits, symmetric dimethylation of the conserved Arg85 of 49 kDa as well as phosphorylation of the Ser36 of 42 kDa subunit (Figure S7a,c). It was suggested that the phosphorylated Ser36 would clash with nucleotide binding by 42 kDa subunit, a nucleoside kinase homologue, as described in the mouse complex I (*8*). However, in the density present in the binding pocket, we could model a molecule of AMP, which is smaller than ADP modelled in the mouse complex (Figure S7a).

Finally, we observed a highly coordinated (four backbone oxygens, a glutamine and one water molecule) cation bound about 7 Å away from FeS clusters N4 and N5. We tentatively assigned the cation as K^+, based on its density (much stronger than water) and distances (~ 2.7 Å) to coordinating oxygen atoms (Figure S7f) (*42*). Presence of the cation in the vicinity of N5, which unusually does not show EPR signal, could be necessary to fine-tune its potential or that of the nearby N4 cluster. The cation probably also stabilizes a very tight turn of the 75 kDa loop between the N4 and N5 clusters.

NADH binding

In all datasets containing NADH (NADH, turnover and rotenone) a clear NADH density was resolved in the same position near FMN as in *T. thermophilus* (Figure S10e) (*43*). It was reported based on the NuoEF subcomplex crystal structures from *Aquifex aeolicus* that the peptide bond 51kDa_Glu99-Gly100 flips away from FMN when the subcomplex is reduced by NADH, as a mechanism to prevent ROS production (*44*). However, C=O bond is always facing away from FMN in ovine enzyme in all the datasets of sufficient resolution, whether the enzyme is reduced or oxidized (Figure S10f,g). This casts doubts over the proposed mechanism (*44*) and the difference could be because of substitution of serine for glycine at position 100 in ovine complex I or the effect of working with a subcomplex in *A. aeolicus*.

Open classes from NADH dataset on the whole appeared slightly more closed than in the native dataset, possibly due to a more pronounced disordering around the Q site seen in native dataset (49 kDa and ND1 loops are disordered). Furthermore, while the N-terminal part of the ND3 loop is ordered in all datasets (residues 27-37), the C-terminal part of ND3 loop (residues 43-48) is disordered in NADH dataset, but ordered in most others.

Rotenone binding

Structurally, inhibition of complex I is not well described and the traditional three classes of complex I inhibitors, A (competitive), B (non-competitive), and C (amilorides, biguanides, capsaicin), were predicted to have distinct binding sites (*45*). In the *Y. lipolytica* complex I structure, a class A inhibitor DQA density was reported in the vicinity of the 49kDa_His59 homologue (*26*). Rotenone, one of the strongest known inhibitors of mammalian complex I and an atypical class B inhibitor, was predicted to bind next to the ND1 loops by photoaffinity labelling studies (*46*). Our structural data confirm that rotenone can bind at both locations, corresponding to the Q_d and Q_s sites. This begins to explain the fact that rotenone was reported to have different K_i values for the active (1 nM) and deactive (80 nM) complex I and that tight binding of rotenone to the active form partially prevents and reverses enzyme deactivation (*23*, *27*). We cannot unambiguously assign the K_i values to each of the three binding sites. The deactive binding site (80 nM) could be the Q_s site or the ND4 site and the other one would represent a hitherto unknown binding site with different binding constants.

Rotenone binding did not change the diameter of the quinone cavity entry or induce massive rearrangements of the quinone cavity as proposed earlier (*24*). Bulky rotenone can thus fit, perhaps with local re-arrangements, through the narrow quinone cavity entry site. This casts doubt on the existence of an alternative access pathway to the N2 cluster proposed earlier, as none of the bulky synthetic quinone derivatives, apart from the largest one, investigated in those studies were significantly larger than rotenone and should therefore be able to fit through the quinone cavity opening (*47*).

Deactive state

The observation of a clearly distinct deactive state structure clarifies why the ovine preparation, which exists mostly in the open conformation had high activity and showed no lag in reaching it, indicating that it was in the active state (Figure S9a-c) (*20*). Open complex I is thermodynamically more stable hence the preparations of complex I which take longer to isolate, involve elevated temperature or employ specific detergents contain more open complex I (*6*, *8*, *18*). In the absence of substrates, the open waiting state can revert into the fully deactive form by ND6 TMH4 tilting and ND6 loop insertion into the PA-MD interface. When NADH or quinone is present, ND6 reorganization is prevented by reordering of ND1 and 49 kDa loops, which interfere with inserted ND6 loop.

Opening of complex I during deactivation was confirmed using the NEM assay, which is the standard biochemical assay for the deactive complex I and depends on testing the liability of the ND3_Cys39 to alkylation (*48*). However, while ND3 accessibility is a good proxy for opening of complex I as it assays the disorder of the ND3 loop, this assay cannot assess the conformational states of the other loops and we use it here strictly to assay the "openness" of complex I. On the other hand, the other known signature A/D feature, the delay in reaching maximal activity upon NADH addition to pre-equilibrated lipid-protein-quinone mixture is indeed a clear indicator of the A/D state of the enzyme. While the deactivated enzyme has consistently shown a significant lag, our standard preparations did not show any delay (Figure S9c), confirming that in all our datasets (apart from the deactive) the protein represents the active enzyme.

According to the NEM assay the ND3 loop was disordered in virtually all the deactive particles and in ~80% of the native particles, consistent with the structural data (Figure S9a). Interestingly, activating isolated complex I with 5 μM NADH (and 200 μM DQ) did not result in a higher proportion of ND3 loop being ordered, also consistent with our structural data from the turnover sample. Since during the preparation of the turnover sample the reaction was allowed to proceed for 20 s before freezing the sample, if activation or catalytic activity were involved in "closing" of the complex, significant difference from the native/NADH closed proportion would be observed. This again confirms that openness of complex I is not correlated with the deactive state, but is an intrinsic property of the sample, with open/closed ratio reflecting the thermodynamically more favorable open state co-existing with the less favorable, but accessible, closed state.

Interestingly, when activating submitochondrial particles, we achieved 40% closed complex I upon activation. This indicates that the lipid membrane is probably necessary for a sustained closing of complex I, e.g. via effects on ordering of the 39 kDa amphipathic helix or through lateral tension of the lipid bilayer on the ND1 subunit. If the proton pumping into the IMS happens mostly in the closed step as predicted by our mechanism, closed state may be more populated after the establishment of a high proton motive force.

Quinone cavity

In NADH and native datasets, we observed density bound near the quinone binding cavity entry, which appeared stronger in the open than in the closed classes (Figure S8e). There is a weaker density bound in a similar position in the native complex I (Figure S8e). We cannot unambiguously assign these densities as they could come from lipid, detergent or native quinone (in the case of native complex) or quinol (in the case of NADH dataset). Density in a similar position has also been reported in *Y. lipolytica* and has been hypothesized to correspond to a negatively charged lipid headgroup (*29*) and more recently to a native quinone (*28*). Based on the appearance, connectedness and strength of these densities, we modelled quinol into the NADH-open complex I but not in the other classes.

None of the classes contained a quinone bound in the position #2 as observed in *Y. lipolytica*, or in position #3, as predicted by MD, presumably because these states are much more shortly lived than the others or are species-specific (*14*, *29*).

Our results do not support the quinone shuttling mechanism (*11*, *24*). UQ_{10} bound in the Q_d site would clearly occlude with its long tail the entire cavity along with the shallow binding site (Figure 4f), preventing binding of second UQ_{10} (*4*, *13*).

The closed cavity is very tight, clearly excluding the possibility of quinone protonation by the bulk solvent. In the open complex I the quinone cavity becomes possibly accessible to bulk solvent near the ND3 loop (although that may still be closed by a disordered loop) and also through an extra cavity passing by ND1_Arg134. Since the ND4L to Q cavity water wire is disrupted in the open state, and quinone can be reduced only in the closed state, this will not de-couple protonation of key ND4L glutamates from quinone reactions. The ND1 loop appears to be a critical coupling element as NADH induces large conformational changes in the ND1 loop, but only when complex I is in the open state. This is consistent with maintaining the correct

stoichiometry of the reaction and with the various decoupling mutations (V208L, E214K and Y215H) observed in the ND1 loop (*4*).

Charge distribution in the membrane domain

Analysis of the putative charges of key residues based on cryo-EM density of open and closed turnover states (Table S7) suggests an asymmetric distribution of charges between the antiporters, with ND4 being out of sync with ND2 and ND5 (Figure 5d). In the open state in ND4, the N-terminal GluTMH5-LysTMH7 pair is neutral, while in ND2 and ND5 this pair is charged. In the closed state the situation is completely reversed. Consistently, LysTMH12 in ND2 and ND5 appear to be non-protonated in the open state while ND4 GluTMH12 is protonated, and the situation is reversed in the closed state. The state of connecting LysTMH8 is not clear from the density but it is likely that they are protonated from the matrix in the open state. Therefore, it is likely that they donate their protons to LysTMH12 in the closed state. The exception to this is the out-of-phase ND4, as ND4_LysTMH8 would have to be protonated in the closed state, accordingly with the state of other key residues. It is likely that the exchange of LysTMH12 for glutamate in ND4 is the primary driver for such an out-of-phase operation. The charge is not clear for all of the key residues from the density itself, however, the distribution in Figure 5d is the most consistent with the available observations while also ensuring that the overall charge within each subunit and the overall nature of interactions is conserved.

ND5-only proton pumping

Due to the extreme difference in the IMS-side hydration between ND5 and other antiporters revealed in this work, it is feasible that all four pumped protons are ejected via ND5, transported there along the central axis (ND5-only model). Low IMS-side hydration in ND2 and ND4, in contrast to high hydration in ND5, have also been noted in earlier MD studies, but the proposal was that some temporary connections to IMS must still be formed in ND2/4 (*49*, *50*). On the other hand, similar considerations led to ND5-only-type model, but in the context of large conformational changes within antiporters (*51*).

In support of ND5-only model, apart from the key half-channel residues, each antiporter contains additional conserved histidines between the connecting and terminal key residue – His186 in ND2, His293 and His319 in ND4, and His328, His332 and Lys336 in ND5. LysTMH8 is replaced in ND5, uniquely, by conserved His248. These increasing amounts of histidines may serve as temporary storage of protons before they can be ejected from ND5 or transferred towards ND5. That way the accumulating positive change in the C-terminal half-channels (+2 in ND2 due to LysTMH12 and His186, +3 in ND4) might in principle provide the necessary driving force to eject four protons from ND5 in one go. However, such accumulation might cause significant electrostatic imbalance in the MD, so the other possibility would be for ND5 to eject protons one by one in quick succession as they arrive, with histidines serving as a back-up in the case of a bottleneck.

Additional arguments for the ND5-only model come from sequence conservation among a wide range of species from prokaryotes to eukaryotes. ND5 subunit, despite being distal, is by far the most conserved of antiporter-like subunits, while ND2 is the least conserved (Figure S8 in (*5*)). This would be expected if ND5 had a different,

controlling role as compared to ND4/ND2. Furthermore, ND5 shows very high conservation all the way from the matrix surface to the IMS surface, while ND4 and ND2 are mostly conserved around the central axis (Figure S6a in (*5*)). Also, in contrast to ND2 and ND4, TMH11 is highly conserved only in ND5, containing two histidines and a lysine in a ladder linking LysTMH12 with HisTMH8.

From a rich compendium of site-specific mutations studied so far (Table S6 in (*5*), checked against recent publications), most of mutations, which allow normal assembly of the enzyme but critically affect activity and proton pumping, are in the key GluTMH5, LysTMH7, LysTMH8 and Lys/GluTMH12 residues. Such mutations would be expected to disrupt both one-proton-per-antiporter and ND5-only modes of proton pumping (as all of these residues are on the central axis) and so do not allow to differentiate between the two. Both models can also explain why mutations in antiporters can affect oxidoreductase activity, as in the case of one-proton-per-antiporter model tight conformational coupling may arrest the conformational changes in ND1, while in the ND5-only model a disrupted central axis may prevent re-protonation of both key ND4L residues and quinone. Thus, again, mutations to key antiporter residues do not differentiate the two models. Mutations of the histidines between LysTMH8 and Lys/GluTMH12 only modestly affect activity and proton pumping (*5*). This would also be consistent with both modes, as these residues likely serve as temporary storage connecting key residues in both cases. Surprisingly, conserved ND4_His220 and ND5_His248, which are likely to play a role in controlling proton access from the matrix, have not been mutated yet.

Mutations supporting the ND5-only model affect residues unique to ND5. Mutations of the conserved Lys336, connecting HisTMH8 and LysTMH12 only in ND5, severely affect both activity and proton pumping (*52*). The conserved Asp393 links LysTMH12 to IMS, and its mutation to alanine results in 50% drop in proton pumping efficiency (*53*). This is a remarkable result since ND5_Asp393 is close to the protein surface and is not present in ND2/4. One result apparently in contradiction with the ND5-only model comes from *Y. lipolytica* mutant which lacks the distal pumping module (ND4/5) and yet apparently pumps two protons per cycle (*54*). However, a possible interpretation is that since the proteinaceous isolation between ND4/ND2 has been lost in the mutant, ND2 LysTMH12 is exposed close to the lipid surface similarly to the wild-type ND5 LysTMH12, and so the remaining two proton pumps can use this site as an alternative proton efflux pathway into the IMS. In bacteria, the deletion of the ND5 homologue completely prevents the assembly of the complex (*53*, *55*), with one contradictory report (*56*). When we removed ND4/5 homologues from the intact *E. coli* enzyme biochemically, the oxidoreductase activity was completely lost (*57*). This would be consistent with the ND5-only model, suggesting that the disrupted ND4/ND2 interface might be either “leaky” to the IMS or not, depending on the species.

Another piece of evidence supporting the unique role of ND5 comes from studies on complex I-related NDH complex. In cyanobacteria this complex exists in several versions with a common core from PA till ND2 subunit homologue (*58*). NDH-1L version has a standard ND5 subunit and is likely involved in proton pumping. NDH-1MS complex specializes in carbon concentration and has a modified ND5 subunit, with the charged residues in LysTMH12-HisTMH8 proton pathway replaced by hydrophobic residues forming a path for CO_2 translocation across the membrane (*59*). This suggests that unlike

other antiporter-like subunits, ND5 can be adapted to translocate either protons or CO_2 and still be driven by the rest of the complex.

Further targeted mutagenesis studies would be needed to fully distinguish between the ND5-only and one antiporter-one proton models. Since the two pathways overlap in the central axis area, mutations will probably need to involve several key residues at a time and experiments should include careful proton pumping measurements.

Entire catalytic cycle

Since the electron transfer rates are fast and the overall reaction is limited by quinone binding/quinol release (*30*), we assume that in most steps the enzyme will be kept reduced. The enzyme cycles between the open and the closed conformations, with most steps in the open state, consistent with its prevalence in the data (Figure S11). The catalytic cycle of complex I begins with quinone binding into the cavity of the open enzyme (state 1, represented in our study by open native classes). Quinone binding will promote the transition into the closed conformation in which the ND1 and 49 kDa loops reorder into the "down" and "retracted" conformations, PSST loop is raised, and quinone moves into the deep site, where it will get reduced (state 2, closed turnover class). This can only happen when the complex is in the closed conformation and the 49 kDa loop is retracted. Quinone reduction and protonation leads to the accumulation of negative charges on the proton donors, 49kDa_Tyr108/Asp160/His59. The overall result of these redox reactions is a conformational (ND6 TMH3 rotation, water wire formation) and electrostatic (de-protonation of key ND4L glutamates) signal towards the E-channel (Supplementary Movie 1). Electrostatics then drive proton translocation in antiporters as in Figure 5d. Subsequent diffusion of quinol out of the deep site towards the shallow site causes disordering of the 49 kDa, ND1 and ND3 loops as well as re-formation of the □-bulge in the ND6 subunit and the opening of the entire complex (state 3, open turnover classes). At this stage, complex I gets fully reduced again, the 49 kDa loop gets extended and the ND1 loop flips upwards, helping to eject the quinol (State 4, open NADH classes). How extensively these loops re-arrange to promote quinone movements is visualized in the Supplementary Movie 2. The re-protonation of the key central axis residues from the matrix side can possibly be happening at States 3, 4 or 1, but we depicted it at State 4 as it is probably the most long-lived state (enzyme waiting for quinone availability). Complex I is thus reset into the "open waiting state" in which it can bind quinone again and restart the catalytic cycle (state 1, native open state). If there is no quinone or NADH present, this state will slowly convert into the deactive state in which the ND6 TMH4 tilts and loop insertion between the PA and MD arrests the open conformation (state 5, deactive open classes).

Comparison with previously proposed mechanisms

Overall, the fact that, under turnover conditions, we do not see conformational changes in the antiporters but see instead a change in the charge distribution in key residues would argue in support of a electrostatic wave type of the mechanism rather than conformational coupling with LysTMH7 taking on protons directly from the matrix side (*4*). However, the mechanism which we propose on the basis of our findings is radically different from the earlier models of electrostatic waves (*15*) because the electric "pulse" in our model originates from proton transfer from the E channel towards quinone. In the

Verkhovskaya model, the driving force was proposed to come directly from negative charge on quinone. Additionally, in our mechanism, the conformational coupling via ND6 TMH3 rotation clearly plays a key role in the E-channel re-arrangements leading to this proton transfer, so our new model is of mixed type – conformational coupling in the E-channel and electrostatic in the antiporters. We do not fully exclude yet a role for conformational coupling in the antiporters, as it is possible that the full conformational change can be achieved only in the lipid bilayer or in the presence of the proton motive force. Furthermore, conformational changes within antiporters could be temporary and high-energy and correspond to a transition state accessible only when the ND6 π-bulge is being formed (*51*). One common feature with the Verkhovskaya model is that, based on the consideration of electrostatics, it also proposed out-of-sync operation of ND4.

A more detailed model developed on the basis of MD simulations from the Kaila group (*16*, *17*, *60*) involves "forward" and "backward" electrostatic waves but no out-of-sync operation of ND4. It was proposed that quinol formation leads to the protonation of undefined charged residues in the ND1/E-channel area, which then opens the Glu-Lys ion pair in ND2, starting a "forward" wave. Opening of the Glu-Lys pairs in each antiporter-like subunit triggers proton transfer to LysTMH12 by destabilizing LysTMH8. The proton transfer is controlled by the hydration state of the channels, which in turn is regulated by the charge state of key residues and involves some conformational changes in the broken helices (*17*). A 'backwave' signal from ND5 towards ND1 is then proposed, in which proton uptake from the matrix and closing of the Glu-Lys pair releases to IMS the proton loaded in the neighboring subunit. The main similarity to our mechanism is the key role for electrostatics and the proposal that Glu-Lys pairs control proton transfer between LysTMH8 and LysTMH12. However, we suggest that instead of opening/closing of pairs the control is exerted through proton exchange between Glu and Lys. This is supported by our observations on the changes in the charge distribution under turnover (Figure S9f-i) and the absence of even local conformational changes in antiporters, in contrast to the very large displacements predicted for Glu-Lys pairs from MD (*60*). Proton transfer within these pairs is probably also a more robust way to achieve consistent switching of channels. Furthermore, instead of the forward and the reverse electrostatic waves, in our mechanism proton translocation proceeds via two forward electrostatic waves driven first by the protonation and then by the de-protonation of ND4L glutamates. One of the key novel features in our mechanism is that quinone oxidoreduction drives this protonation via defined conformational changes in ND1/E-channel, including large displacements of Q cavity loops, ND1 helices tilt, ND6 TMH3 rotation and formation of the water wire to ND4L. In that way quinone "charge action" is delivered directly to the first antiporter ND2, starting the electrostatic wave propagation.

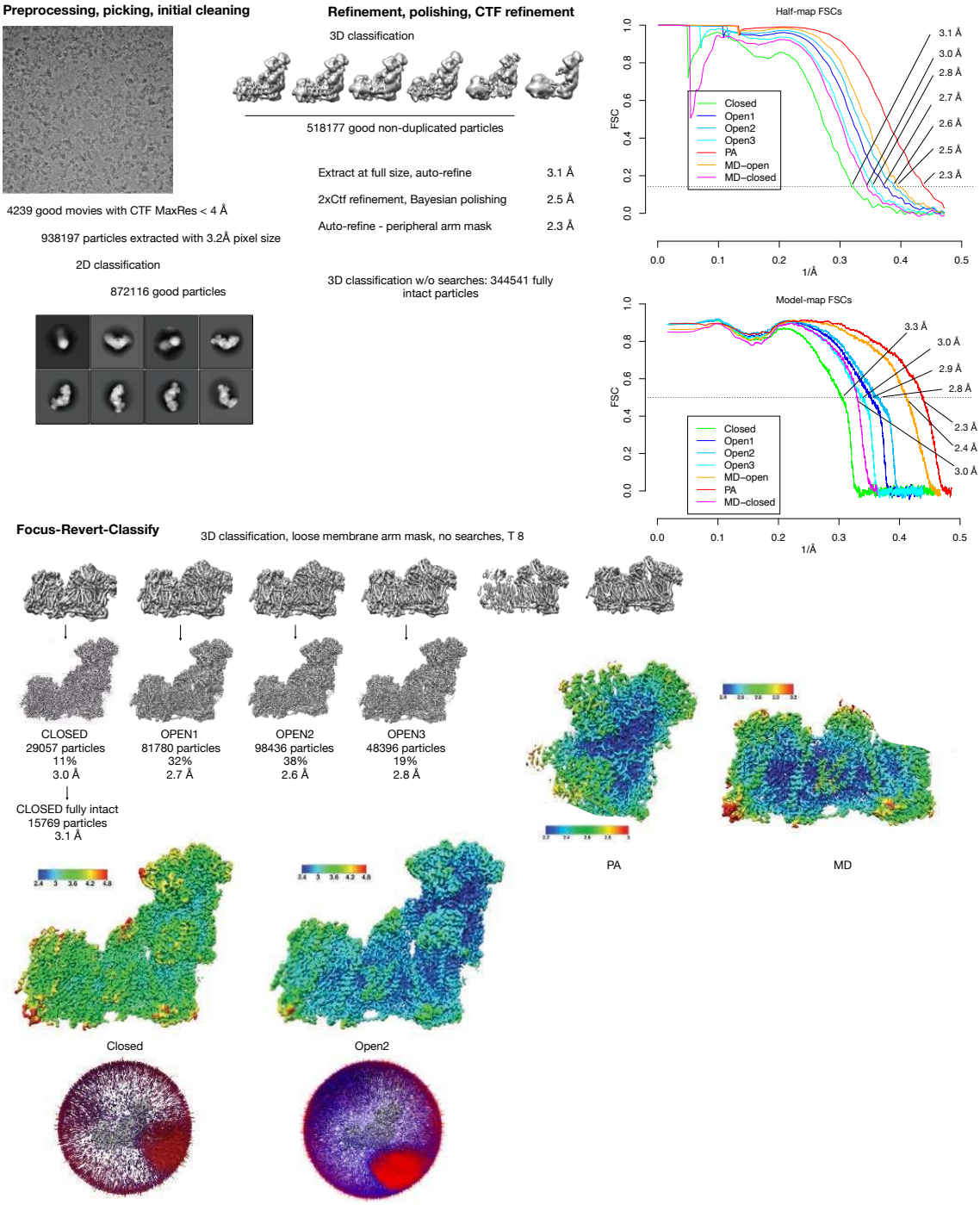

Fig. S1. Processing of the turnover cryo-EM dataset.

Processing pipeline and FSC plots of the turnover dataset. Local resolution maps and angular distribution plots of the closed and open2 classes are shown, as well as local resolution maps of the focus-refined PA and MD.

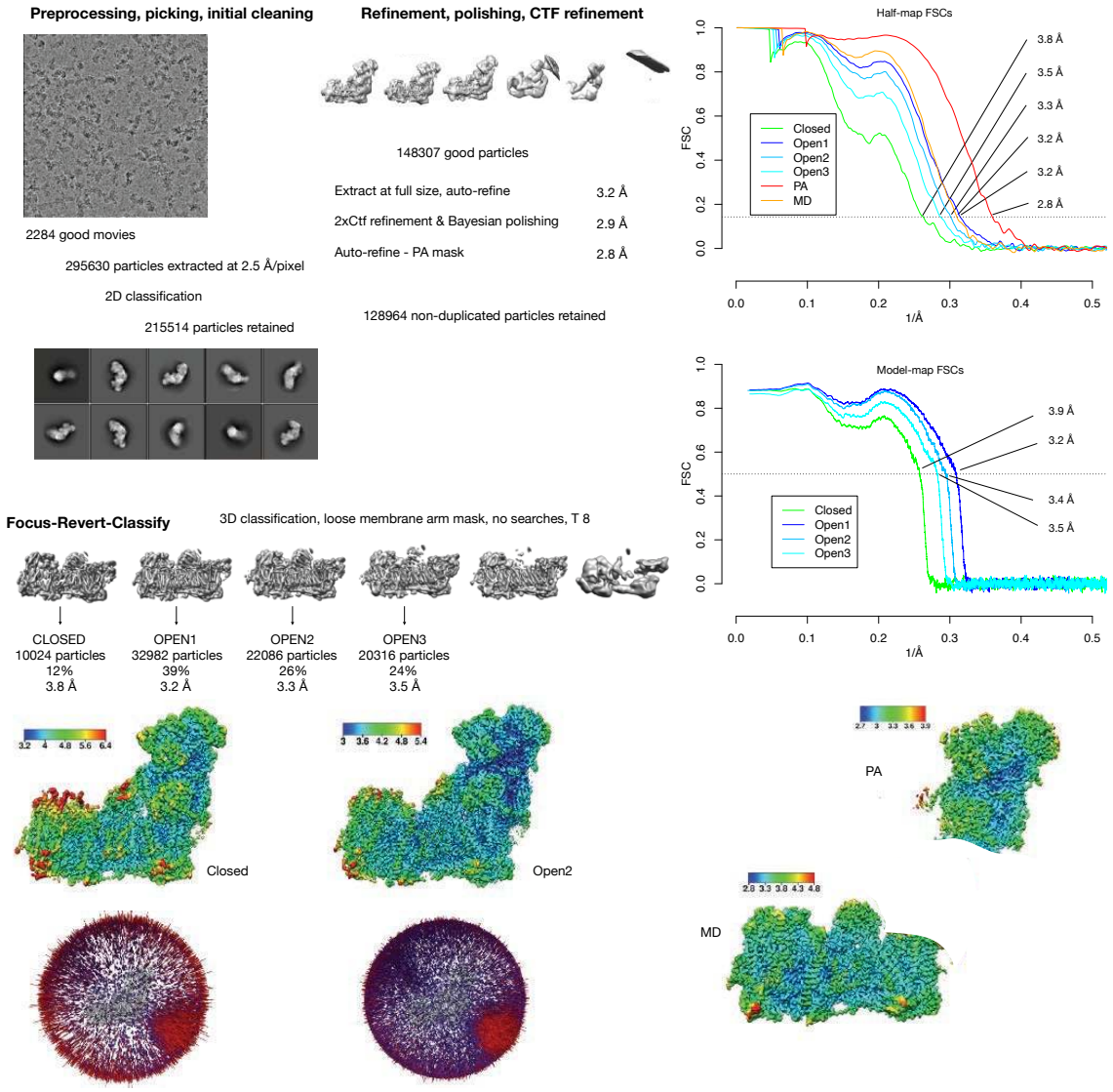

Fig. S2. Processing of the native cryo-EM dataset.

Processing pipeline and FSC plots of the native dataset. Local resolution maps and angular distribution plots of the closed and open2 classes are shown, as well as local resolution maps of the focus-refined PA and MD.

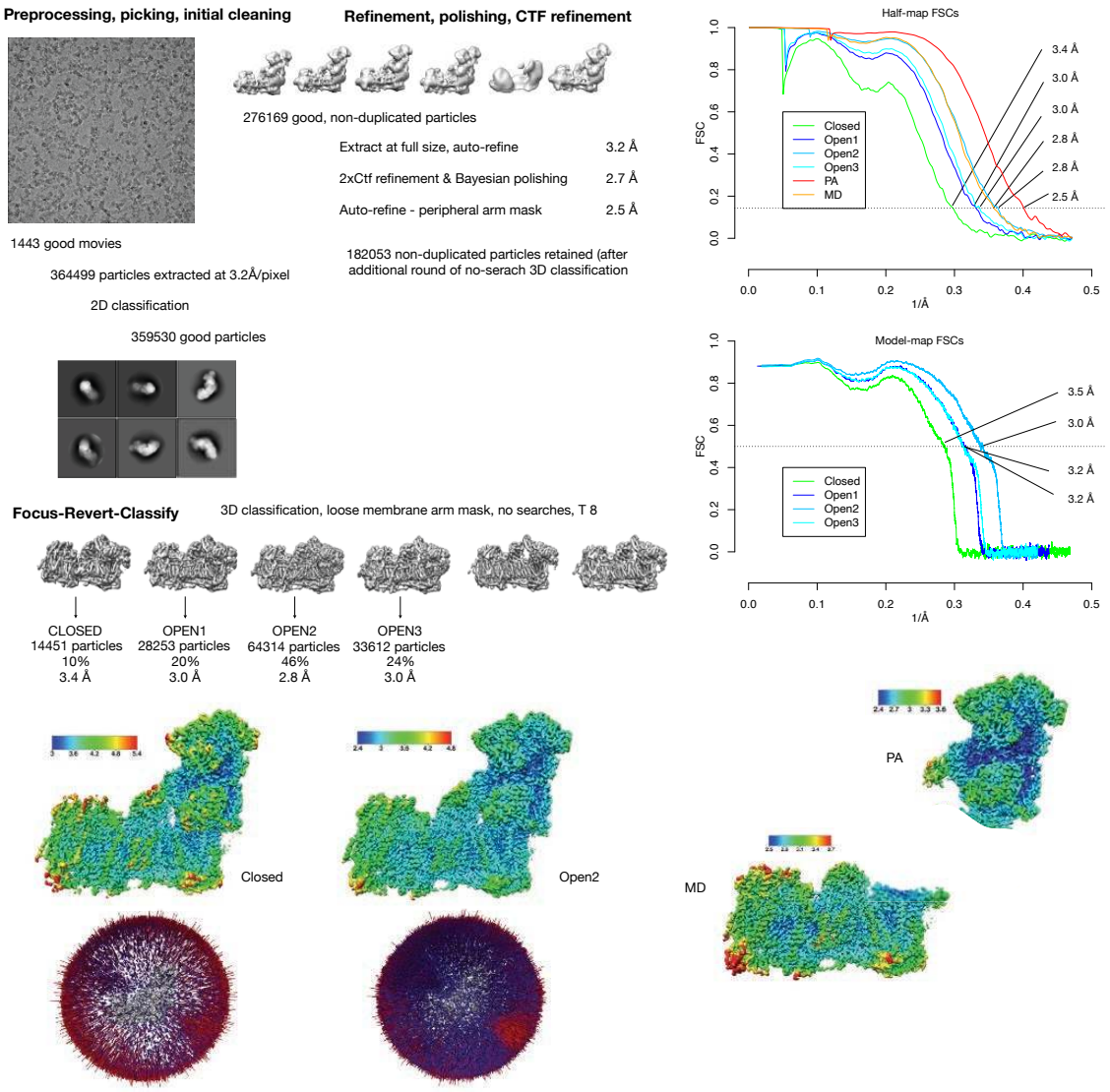

Fig. S3. Processing of the NADH cryo-EM dataset.

Processing pipeline and FSC plots of the NADH dataset. Local resolution maps and angular distribution plots of the closed and open2 classes are shown, as well as local resolution maps of the focus-refined PA and MD.

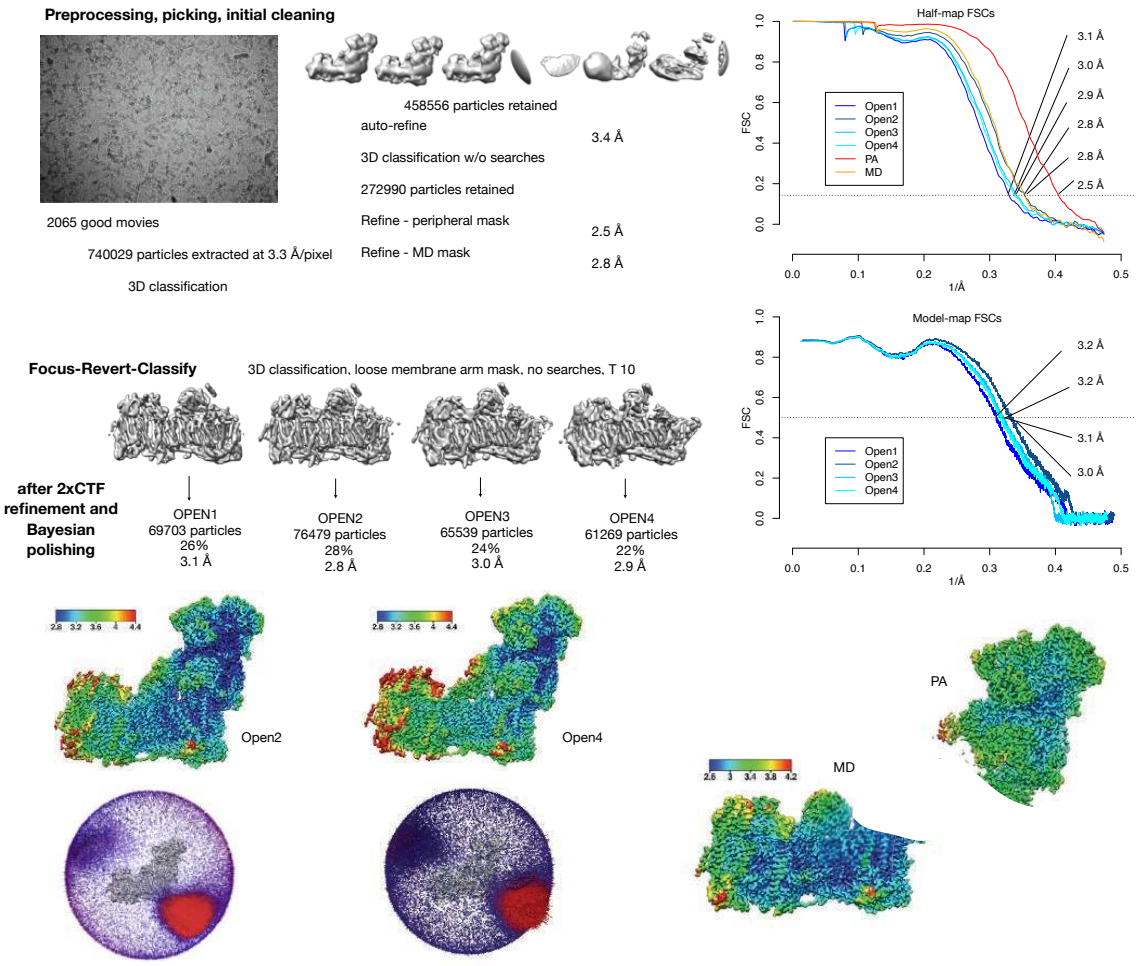

Fig. S4. Processing of the deactive cryo-EM dataset.

Processing pipeline and FSC plots of the deactive dataset. Local resolution maps and angular distribution plots of the open2 and open4 classes are shown, as well as local resolution maps of the focus-refined PA and MD.

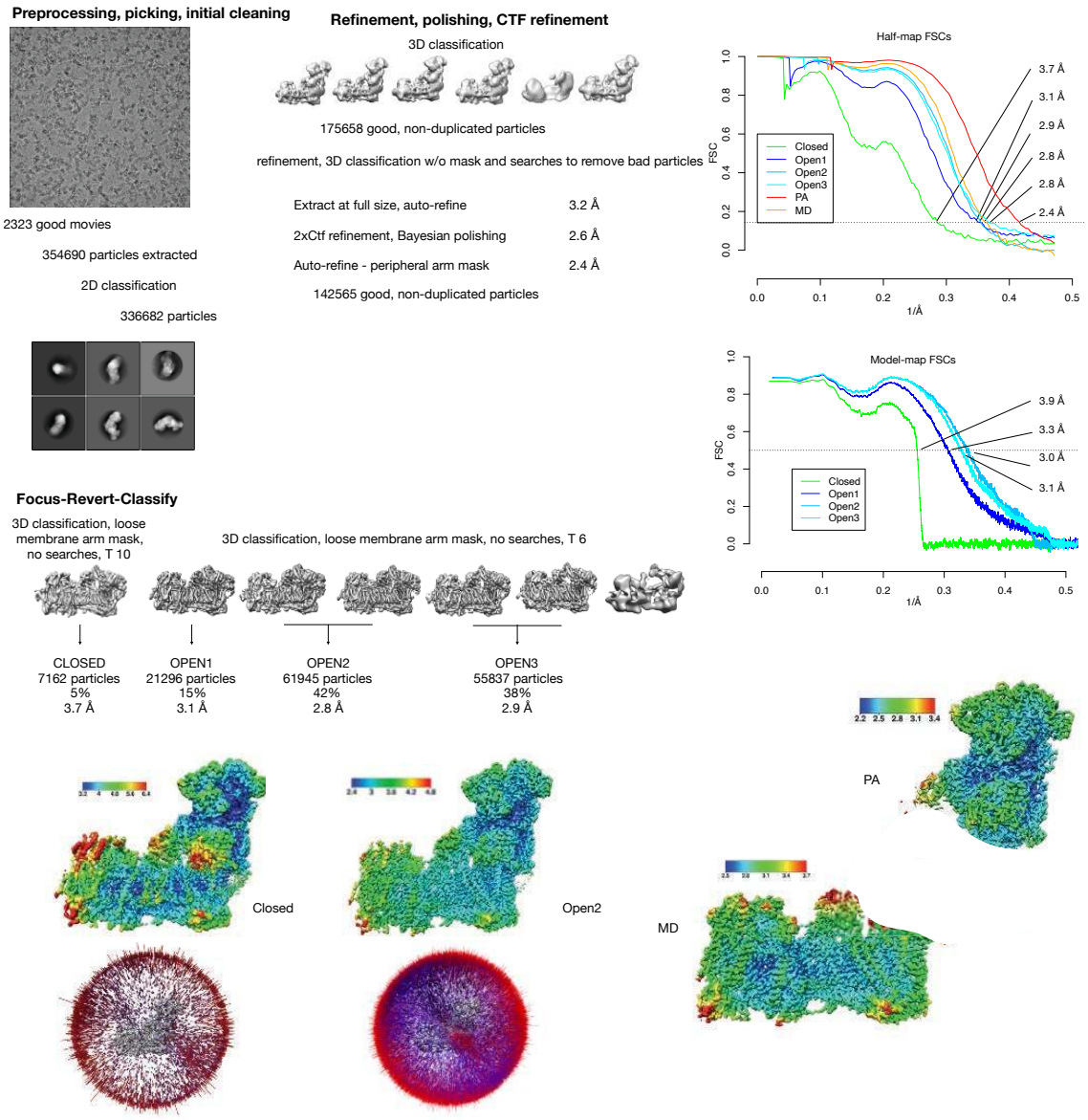

Fig. S5. Processing of the rotenone cryo-EM dataset.

Processing pipeline and FSC plots of the rotenone dataset. Local resolution maps and angular distribution plots of the closed and open2 classes are shown, as well as local resolution maps of the focus-refined PA and MD.

.

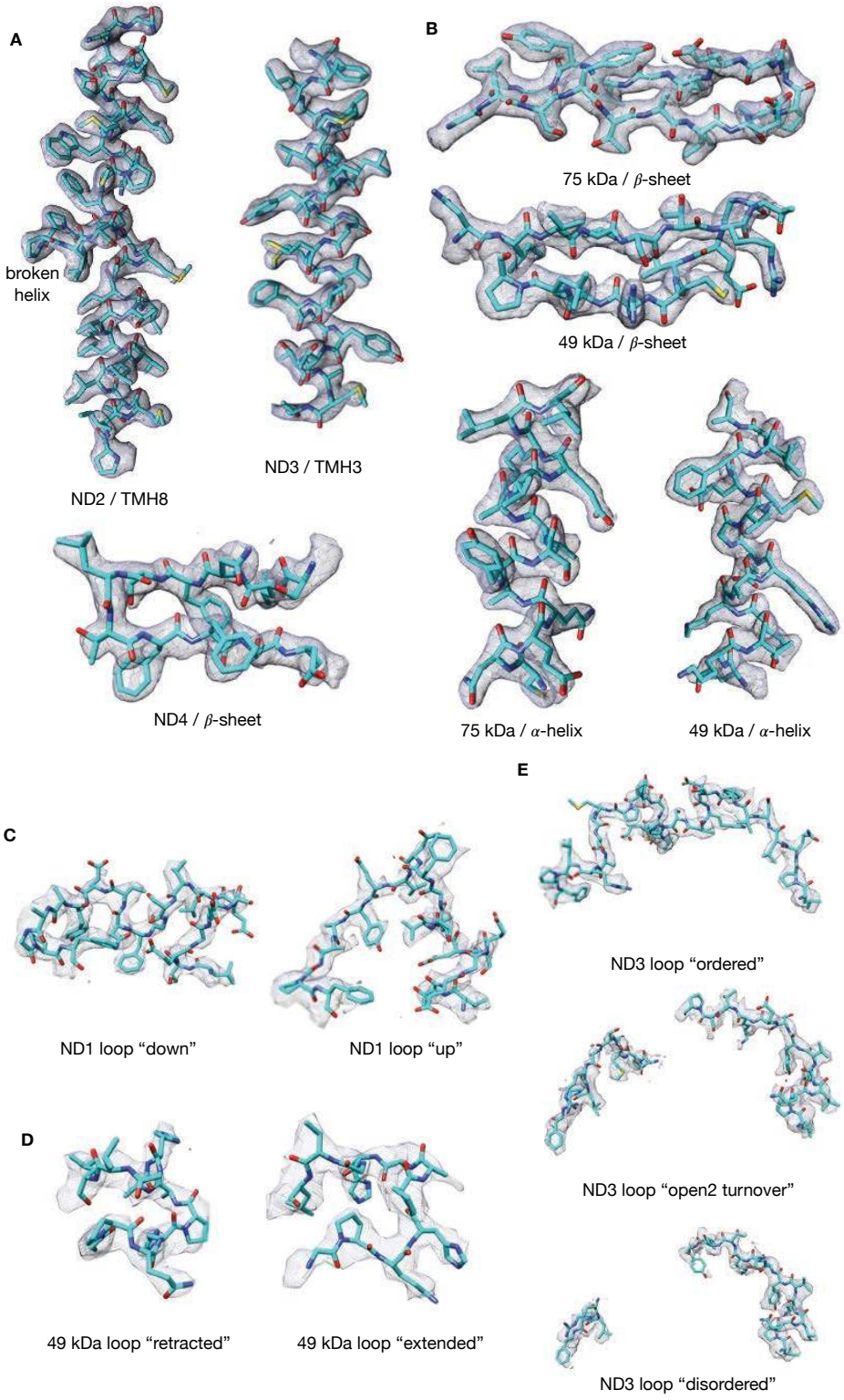

Fig. S6. Cryo-EM density examples of polypeptides.

a. Density in various regions of the MD focus-refined map from the turnover dataset shown at 4 σ contour level. **b.** Density in various regions of the PA focus-refined map

from the turnover dataset shown at 4 σ contour level. **c.** Densities for the ND1 loop in the "down" conformation (Turnover closed class, left-hand side) and the "up" conformation (NADH open2 class, right-hand side) shown at 2 σ contour level. **d.** Density for the 49 kDa loop in the retracted (Turnover closed class, left-hand side) and in the extended conformation (NADH open2 class, right-hand side) shown at 2 σ contour level. **e.** Density for the ND3 loop in the fully ordered (turnover closed class, top), partially disordered (open2 turnover class, middle) and disordered conformation (NADH open2 class, bottom) shown at 2 σ contour level.

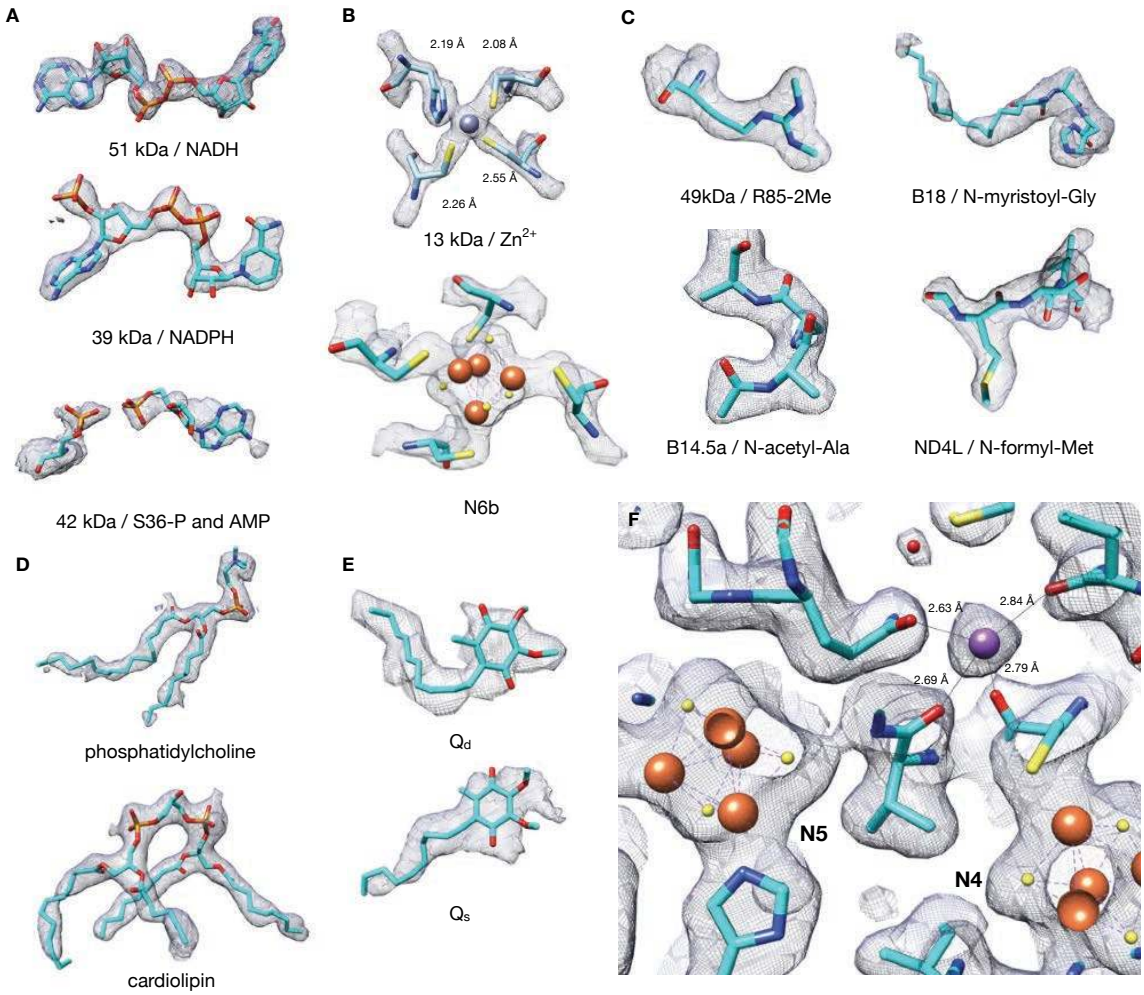

Fig. S7. Cryo-EM density examples for ligands.

a. Densities for bound nucleotides at contour levels 3 σ for NADH, 4 σ for NADPH, and 2 σ for AMP. **b.** Densities for Zn^{2+} at 5 σ contour level and iron-sulfur cluster N6b at 3 σ contour level. **c.** Densities for various post-translational modifications at contour levels of 3 σ for B14.5a and 49 kDa, 2 σ for ND4L and 1.8 σ for B18. **d.** Densities for lipids at 2 σ contour levels. **e.** Densities for quinones at 1.3 σ contour levels. **f.** Density for the putative K^+ ion binding next to N5 and N4 clusters at 3 σ contour level.

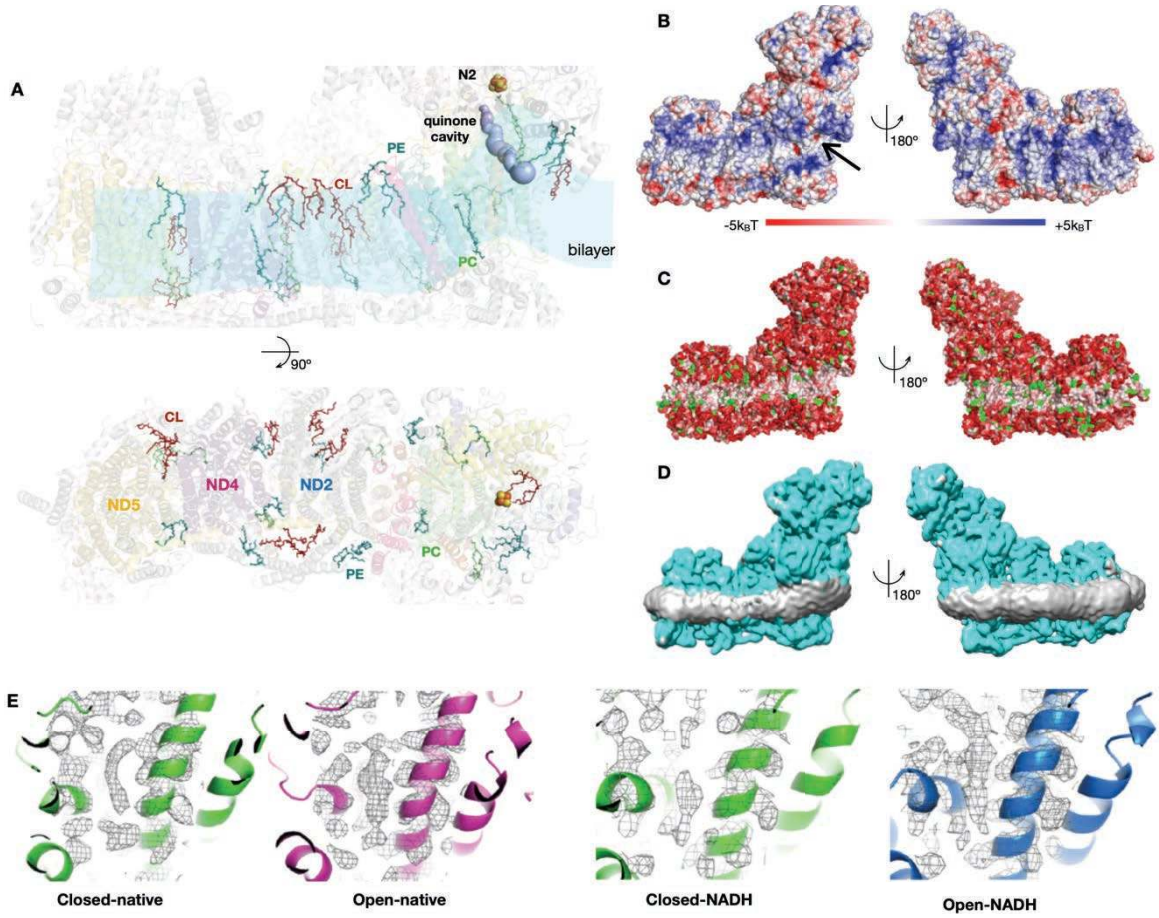

Fig. S8. Interactions with quinone and lipids.

a. Lipids modelled into the complex I structures shown as sticks: phosphatidylethanolamine (blue), cardiolipin (red) and phosphatidycholine (green). The approximate boundaries of the lipid bilayer based on the lipid headgroup positions are shaded in cyan. **b.** Surface electrostatic potential of complex I reveals many lipid binding sites, negatively charged quinone entry site and membrane curvature around quinone entry point. **c.** Hydrophobicity plot of complex I with white regions showing hydrophobic and red regions showing hydrophilic residues reveals the transmembrane region. Tryphophan and tyrosine residues, which often denote membrane edge are shown in green. **d.** Open2-turnover structure filtered to 8 Å reveals curvature of the detergent belt around the quinone entry site (indicated). **e.** Comparison of the densities (all shown at contour level of 1.5 σ) near the entry into the quinone cavity in closed native complex (green) vs. open native complex (magenta) and closed NADH complex (green) vs. open NADH complex (blue). NADH open state has the strongest density, which was modelled as quinone.

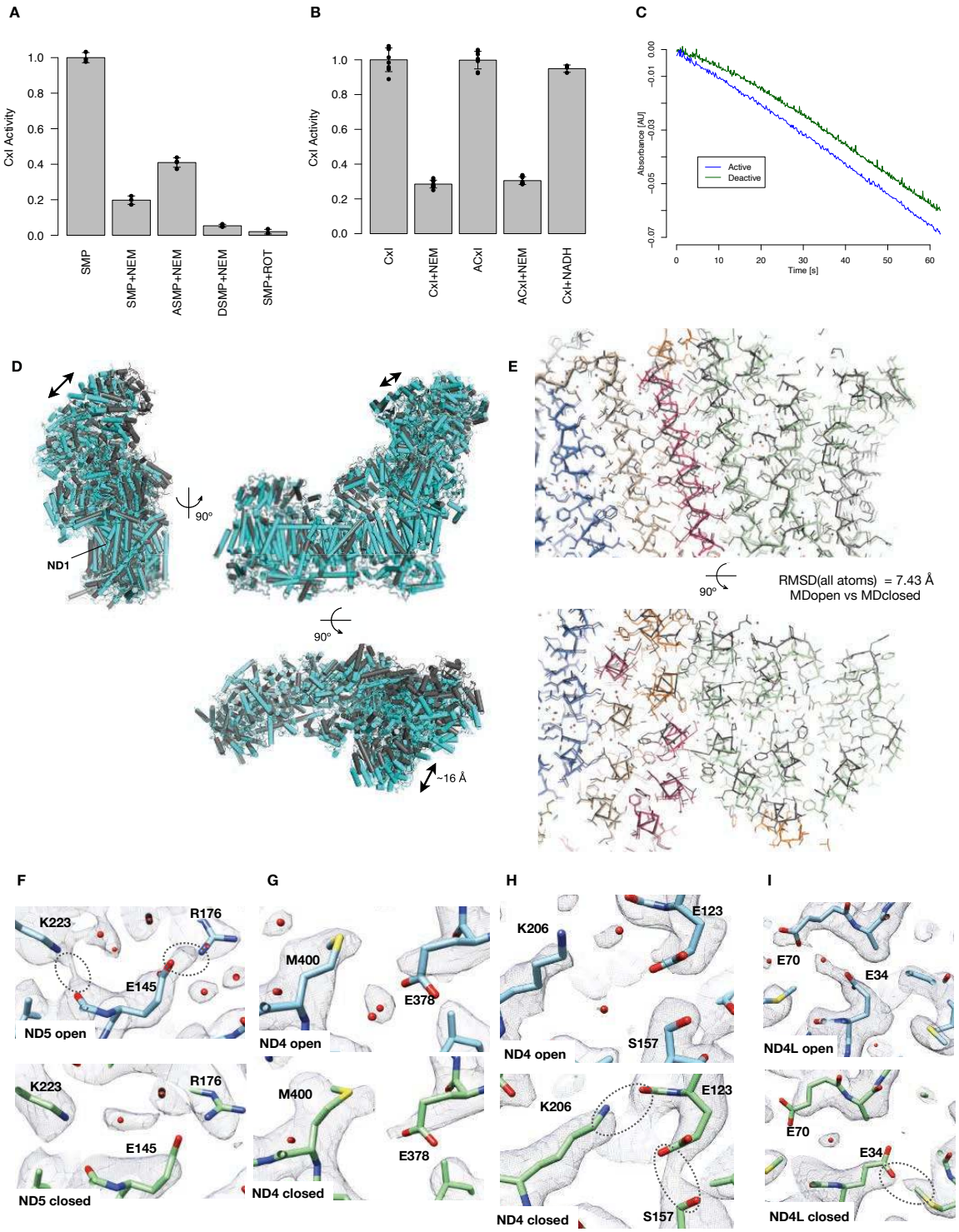

Fig. S9. Deactive complex I is inhibited by NEM and shows a lag in reaching maximal activity (a-c); comparison of closed and open states of complex I (d-i).

a. Complex I within SMPs is ~20% closed, which increases to ~40% closed upon activation with 5 μM NADH and 200 μM DQ (ASMP), while deactivation of SMPs (DSMP) decreases it to ~0%. **b.** Activation of purified complex I (ACxI) does not change

closed/open ratio. 30 min incubation with 5 mM NADH as in the NADH dataset does not inhibit complex I (CxI+NADH). **c.** Deactive complex I shows a lag in reaching maximum activity. Reaction was started by the addition of NADH to complex I preincubated in lipid and DQ containing buffer. **d.** Overall comparison of closed (cyan) and open (grey) complex I reveals tilting of the entire PA and large changes in ND1 subunit. **e.** E-channel in open and closed MD differs radically in tilting and displacements of several helices and different side chain conformations. **f-i.** Detailed analysis of cryo-EM density reveals breaking of several hydrogen bonds and salt bridges (circled) and changes in glutamate carboxyl densities between open and closed MD. This indicates charge differences between these residues. Contour levels shown are as follows: f) open 1.8 σ, closed 1.9 σ, g) open 2.2 σ, closed 2.4 σ, h) open 2.2 σ, closed 1.9 σ, i) open 2.0 σ, closed 1.9 σ.

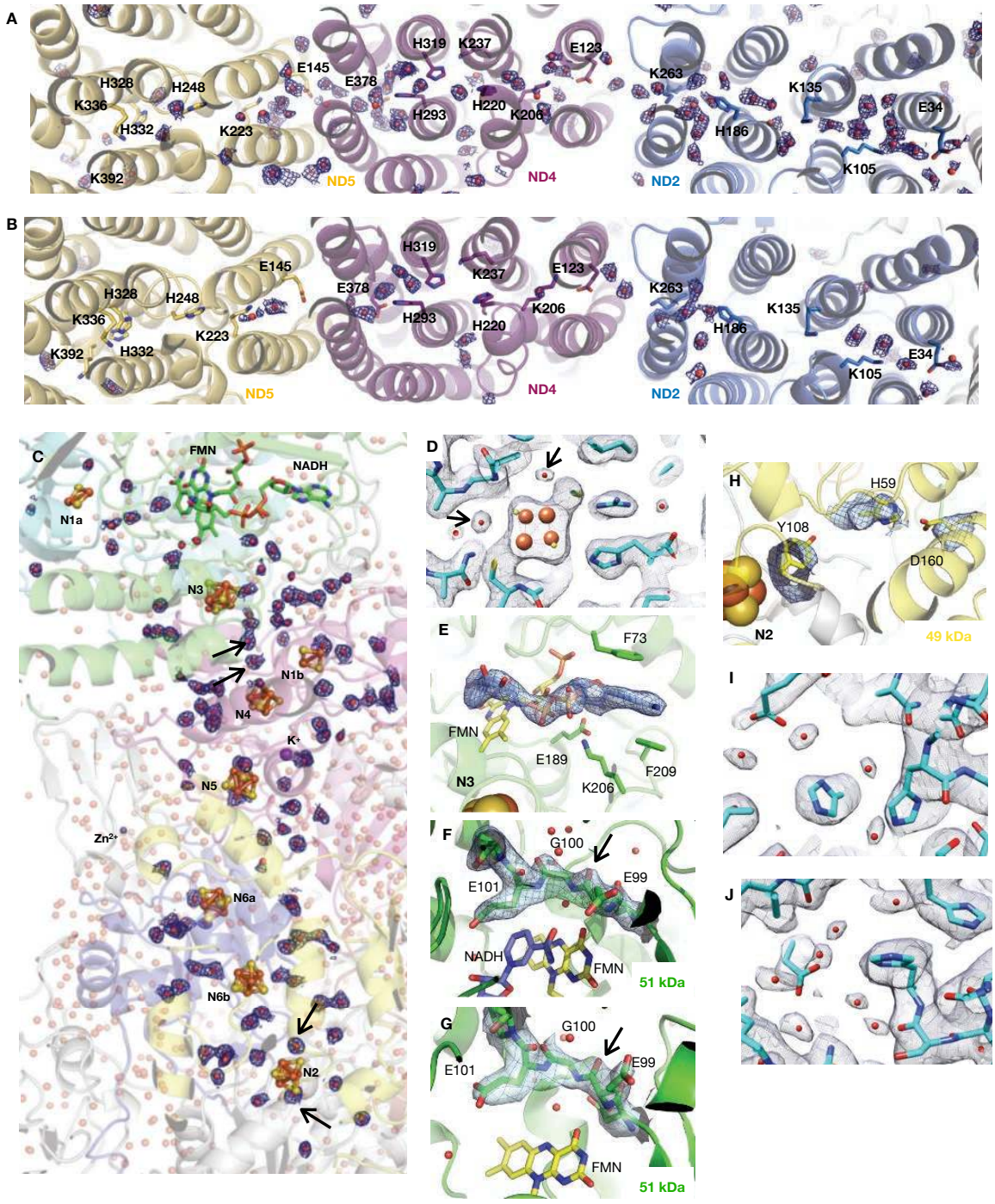

Fig. S10. Water molecules delineate proton pathways in complex I.

a. Central hydrophilic axis with water molecule densities in open MD structure. **b.** Central hydrophilic axis with water molecule densities in closed MD structure. **c.** Peripheral arm, with water molecules within 10 Å of FeS clusters shown as red sphere with corresponding density, with other identified waters in the background. Two water molecules within hydrogen bonding distance to N2 and two molecules between N3 and N4 clusters (i.e. not in a direct N3-N1b-N4 path) are indicated with arrows. **d.** Examples

of water densities at hydrogen-bonding distance from the N2 cluster. **e.** NADH density in the 51 kDa subunit. NADH binds by forming π-stacking interactions between the nicotinamide ring and the FMN as well as between the adenine and Phe73 and Phe206. **f-g.** The conformation of the backbone between residues 98 and 101 remains unchanged in all the models and backbone carboxyl of Gly99 (indicated) faces away from the FMN in all cases. Turnover PA focus-refined map (**f**) and deactive PA focus-refined map (**g**) are shown for comparison. **h.** 49kDa_Asp160 displays weak density and no connection to His59 in all of the classes apart from closed turnover class. NADH closed class is shown for comparison. **i.** Example of water density around ND4_Glu378 in closed MD structure. **j.** Examples of water densities near ND4_E378 in the open MD structure. All the densities are shown at the contour level of 2 σ.

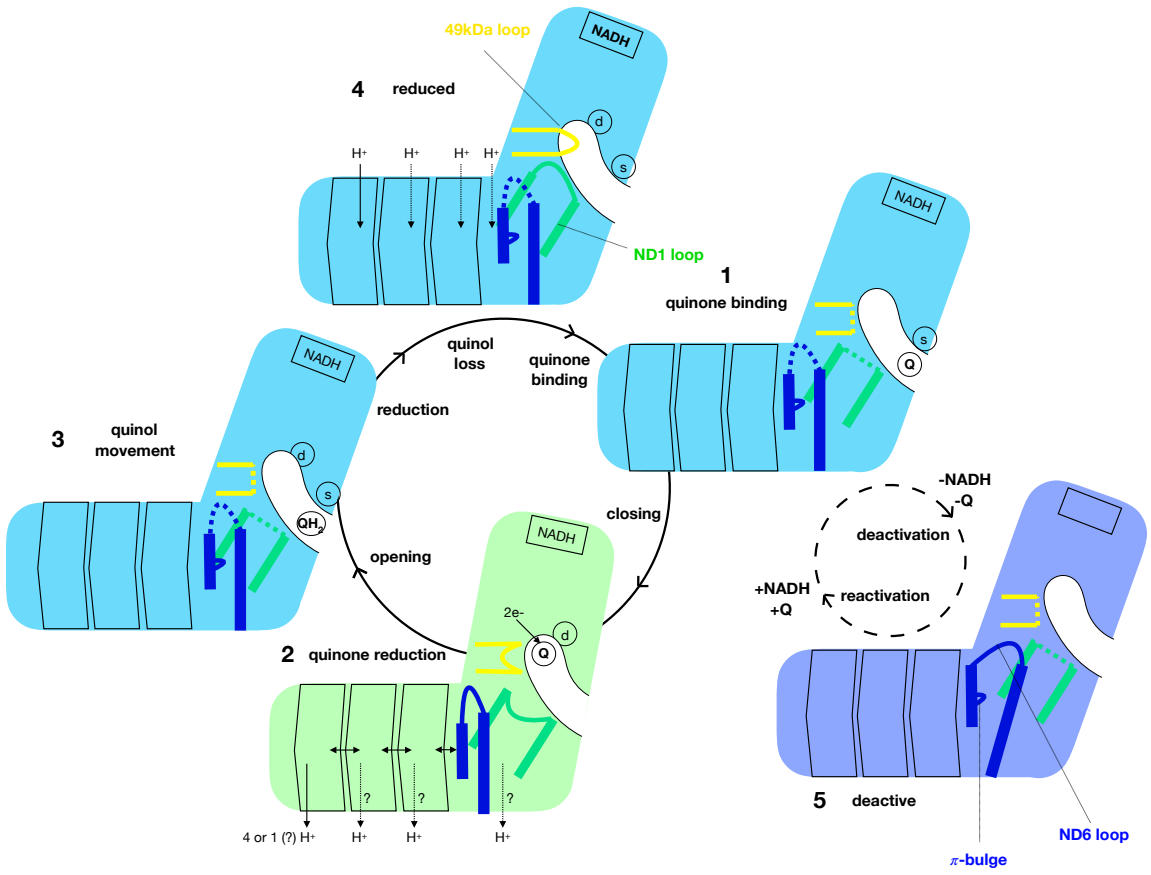

Fig. S11. Proposed full catalytic cycle.

Schematic representation of the main catalytic steps in complex I shows how reduction of quinone and its diffusion in and out of the cavity are coupled to loop movements (ND6 in blue, 49 kDa in yellow, ND1 in green), opening of the complex (open conformations are in blue and closed in green) and pumping of protons. In step 1, quinone binding elicits closing of the complex, which results in ordering of the loops and binding of quinone into the Q_d site where it gets reduced (step 2). Reduction results in proton pumping through the electrostatic wave in the antiporters (horizontal arrows), opening of the complex and initiation of the release of quinol (step 3). Quinol release and uptake of protons are completed by NADH reduction (step 4), which reorders the 49 kDa and ND1 loops in extended conformations. If there is quinone available, the pathway restarts, otherwise complex I in the absence of substrates slowly reverts into the deactive state (step 5).

Table S1

Model and data collection statistics for native complex I dataset

	Native CxI – closed (EMD-11256) (PDB 6ZKO)	Native CxI – open1 (EMD-11257) (PDB 6ZKP)	Native CxI – open2 (EMD-11258) (PDB 6ZKQ)	Native CxI – open3 (EMD-11259) (PDB 6ZKR)	PA-focused refinement	MD-focused refinement
Data collection and processing						
Microscope	Titan Krios	Titan Krios	Titan Krios	Titan Krios	Titan Krios	Titan Krios
Camera	Falcon 3 linear	Falcon 3 linear	Falcon 3 linear	Falcon 3 linear	Falcon 3 linear	Falcon 3 linear
Magnification	165000x	165000x	165000x	165000x	165000x	165000x
Voltage (kV)	300	300	300	300	300	300
Electron exposure (e–/Å^2)	98	98	98	98	98	98
Automation software	EPU	EPU	EPU	EPU	EPU	EPU
Number of frames	40	40	40	40	40	40
Defocus range (μm)	~ -1 to -2	~ -1 to -2	~ -1 to -2	~ -1 to -2	~ -1 to -2	~ -1 to -2
Pixel size (Å)	0.83	0.83	0.83	0.83	0.83	0.83
Symmetry imposed	C1	C1	C1	C1	C1	C1
Number of micrographs	2284	2284	2284	2284	2284	2284
Initial particle images	128952	128952	128952	128952	128952	128952
Final particle images	10024	32982	22086	20316	75384	75384
Map resolution (Å) at 0.143 FSC threshold	3.8	3.2	3.3	3.5	2.8	3.2
Refinement						
Initial model used (PDB code)	5LNK	5LNK	5LNK	5LNK		
Refinement package	Phenix, real space	Phenix, real space	Phenix, real space	Phenix, real space		
Model resolution (Å) at 0.5 FSC threshold	3.9	3.2	3.4	3.5		
Local resolution range (Å)	3.2-6.4	3.0-5.4	3.0-5.4	3.0-5.4		
Cross-correlation						
Mask	0.794	0.880	0.868	0.831		
Volume	0.771	0.851	0..841	0.801		
Map sharpening *B* factor (Å^2)	-72	-56	-61	-67		
Model composition						
Non-hydrogen atoms	67877	67353	67353	67353	-	-
Protein residues	66140	65544	65544	65544		
Ligands	1737	1809	1809	1809		
B factors (Å^2)						
Protein	77	49	57	65	-	-
Ligand	102	75	83	90		
R.m.s. deviations						
Bond lengths (Å)	0.0064	0.01	0.0095	0.0083	-	-
Bond angles (°)	1.22	1.30	1.29	1.28		
Validation						
MolProbity score	1.61	1.48	1.52	1.58	-	-
EMRinger score	2.36	4.50	4.05	3.30		
Clashscore	5.39	4.49	4.40	5.09		
Poor rotamers (%)	0.08	0.13	0.06	0.08		
C-beta deviations	0	0	0	0		
CaBLAM outliers (%)	1.99	1.70	1.69	1.97		
Ramachandran plot						
Favored (%)	95.40	96.18	95.72	95.50	-	-
Allowed (%)	4.58	3.81	4.27	4.50		
Disallowed (%)	0.02	0.01	0.01	0.00		

Table S2

Model and data collection statistics for NADH complex I dataset

	CxI-NADH – closed (EMD-11248) (PDB 6ZKG)	CxI-NADH – open1 (EMD-11249) (PDB 6ZKH)	CxI-NADH – open2 (EMD-11250) (PDB 6ZKI)	CxI-NADH – open3 (EMD-11251) (PDB 6ZKJ)	PA-focused refinement	MD-focused refinement
Data collection and processing						
Microscope	Titan Krios	Titan Krios	Titan Krios	Titan Krios	Titan Krios	Titan Krios
Camera	Falcon 3 linear	Falcon 3 linear	Falcon 3 linear	Falcon 3 linear	Falcon 3 linear	Falcon 3 linear
Magnification	130000x	130000x	130000x	130000x	130000x	130000x
Voltage (kV)	300	300	300	300	300	300
Electron exposure (e–/Å^2)	89	89	89	89	89	89
Automation software	EPU	EPU	EPU	EPU	EPU	EPU
Number of frames	40	40	40	40	40	40
Defocus range (μm)	~ -1 to -2	~ -1 to -2	~ -1 to -2	~ -1 to -2	~ -1 to -2	~ -1 to -2
Pixel size (Å)	1.061	1.061	1.061	1.061	1.061	1.061
Symmetry imposed	C1	C1	C1	C1	C1	C1
Number of micrographs	1443	1443	1443	1443	1443	1443
Initial particle images	182053	182053	182053	182053	182053	182053
Final particle images	14451	28253	64314	33612	182053	126179
Map resolution (Å) at 0.143 FSC threshold	3.4	3.0	2.8	3.0	2.5	2.8
Refinement						
Initial model used (PDB code)	5LNK	5LNK	5LNK	5LNK		
Refinement package	Phenix, real space	Phenix, real space	Phenix, real space	Phenix, real space		
Model resolution (Å) at 0.5 FSC threshold	3.5	3.2	3.0	3.2		
Local resolution range (Å)	3.0-5.4	2.4-4.8	2.4-4.8	2.4-4.8		
Cross-correlation						
Mask	0.812	0.843	0.870	0.844		
Volume	0.794	0.824	0.852	0.827		
Map sharpening *B* factor (Å^2)	-61	-50	-43	-43		
Model composition						
Non-hydrogen atoms	67921	67479	67479	67479	-	-
Protein residues	66140	65603	65603	65603		
Ligands	1781	1876	1876	1876		
B factors (Å^2)						
Protein	68	47	50	50	-	-
Ligand	96	72	76	76		
R.m.s. deviations						
Bond lengths (Å)	0.0074	0.0080	0.0089	0.0074	-	-
Bond angles (°)	1.25	1.26	1.28	1.24		
Validation						
MolProbity score	1.62	1.55	1.53	1.54	-	-
EMRinger score	3.31	3.97	4.58	4.05		
Clashscore	5.56	5.16	5.10	5.33		
Poor rotamers (%)	0.06	0.04	0.06	0.07		
C-beta deviations	0	0	0	0		
CaBLAM outliers (%)	1.87	1.72	1.74	1.69		
Ramachandran plot						
Favored (%)	95.44	95.95	96.22	96.27	-	-
Allowed (%)	4.54	4.01	3.72	3.69		
Disallowed (%)	0.02	0.04	0.06	0.04		

Table S3

Model and data collection statistics for deactive complex I dataset

	Deactive CxI – open1 (EMD-11260) (PDB 6ZKS)	Deactive CxI – open2 (EMD-11261) (PDB 6ZKT)	Deactive CxI – open3 (EMD-11262) (PDB 6ZKU)	Deactive CxI – open4 (EMD-11263) (PDB 6ZKV)	PA-focused refinement	MD-focused refinement
Data collection and processing						
Microscope	Titan Krios	Titan Krios	Titan Krios	Titan Krios	Titan Krios	Titan Krios
Camera	K3	K3	K3	K3	K3	K3
Magnification	81000x	81000x	81000x	81000x	81000x	81000x
Voltage (kV)	300	300	300	300	300	300
Electron exposure (e–/Å^2)	79	79	79	79	79	79
Automation software	SerialEM	SerialEM	SerialEM	SerialEM	SerialEM	SerialEM
Number of frames	50	50	50	50	50	50
Defocus range (μm)	~ -1 to -2	~ -1 to -2	~ -1 to -2	~ -1 to -2	~ -1 to -2	~ -1 to -2
Pixel size (Å)	1.055	1.055	1.055	1.055	1.055	1.055
Symmetry imposed	C1	C1	C1	C1	C1	C1
Number of micrographs	2065	2065	2065	2065	2065	2065
Initial particle images	272990	272990	272990	272990	272990	272990
Final particle images	69703	76479	65539	61269	272990	272990
Map resolution (Å) at 0.143 FSC threshold	3.1	2.8	3.0	2.9	2.5	2.8
Refinement						
Initial model used (PDB code)	5LNK	5LNK	5LNK	5LNK		
Refinement package	Phenix, real space	Phenix, real space	Phenix, real space	Phenix, real space		
Model resolution (Å) at 0.5 FSC threshold	3.2	3.0	3.1	3.2		
Local resolution range (Å)	2.8-4.4	2.8-4.4	2.8-4.4	2.8-4.4		
Cross-correlation						
Mask	0.783	0.805	0.816	0.801		
Volume	0.759	0.780	0.790	0.778		
Map sharpening B factor (Å^2)	-87	-84	-73	-81		
Model composition						
Non-hydrogen atoms	66294	66294	65505	65224	-	-
Protein residues	64905	64905	64116	63835		
Ligands	1389	1389	1389	1389		
B factors (Å^2)						
Protein	61	60	56	66	-	-
Ligand	81	80	78	89		
R.m.s. deviations						
Bond lengths (Å)	0.0074	0.0079	0.0089	0.0074	-	-
Bond angles (°)	1.26	1.27	1.30	1.24		
Validation						
MolProbity score	1.54	1.52	1.54	1.49	-	-
EMRinger score	3.67	4.03	3.82	3.53		
Clashscore	5.12	4.84	4.96	4.88		
Poor rotamers (%)	0.10	0.07	0.06	0.06		
C-beta deviations	0	0	0	0		
CaBLAM outliers (%)	1.82	1.94	1.73	1.72		
Ramachandran plot						
Favored (%)	96.13	96.06	95.90	96.39	-	-
Allowed (%)	3.87	3.93	4.09	3.61		
Disallowed (%)	0.00	0.01	0.01	0.00		

Table S4

Model and data collection statistics for rotenone complex I dataset

	CxI-rotenone – closed (EMD-11252) (PDB 6ZKK)	CxI-rotenone – open1 (EMD-11253) (PDB 6ZKL)	CxI-rotenone – open2 (EMD-11254) (PDB 6ZKM)	CxI-rotenone – open3 (EMD-11255) (PDB 6ZKN)	PA-focused refinement	MD-focused refinement
Data collection and processing						
Microscope	Titan Krios	Titan Krios	Titan Krios	Titan Krios	Titan Krios	Titan Krios
Camera	Falcon 3 linear	Falcon 3 linear	Falcon 3 linear	Falcon 3 linear	Falcon 3 linear	Falcon 3 linear
Magnification	130000x	130000x	130000x	130000x	130000x	130000x
Voltage (kV)	300	300	300	300	300	300
Electron exposure (e–/Å^2)	89	89	89	89	89	89
Automation software	EPU	EPU	EPU	EPU	EPU	EPU
Number of frames	40	40	40	40	40	40
Defocus range (μm)	~ -1 to -2	~ -1 to -2	~ -1 to -2	~ -1 to -2	~ -1 to -2	~ -1 to -2
Pixel size (Å)	1.061	1.061	1.061	1.061	1.061	1.061
Symmetry imposed	C1	C1	C1	C1	C1	C1
Number of micrographs	2323	2323	2323	2323	2323	2323
Initial particle images	142565	142565	142565	142565	142565	142565
Final particle images	7162	21296	61945	55837	142565	129794
Map resolution (Å) at 0.143 FSC threshold	3.7	3.1	2.8	2.9	2.4	2.8
Refinement						
Initial model used (PDB code)	5LNK	5LNK	5LNK	5LNK		
Refinement package	Phenix, real space	Phenix, real space	Phenix, real space	Phenix, real space		
Model resolution (Å) at 0.5 FSC threshold	3.9	3.3	3.0	3.1		
Local resolution range (Å)	3.2-6.4	2.4-4.8	2.4-4.8	2.4-4.8		
Cross-correlation						
Mask	0.754	0.738	0.820	0.807		
Volume	0.727	0.723	0.799	0.792		
Map sharpening *B* factor (Å^2)	-100	-44	-71	-48		
Model composition						
Non-hydrogen atoms	67650	67492	65955	65318	-	-
Protein residues	66140	65581	64385	63748		
Ligands	1810	1911	1570	1570		
B factors (Å^2)						
Protein	75	65	59	65	-	-
Ligand	102	91	80	86		
R.m.s. deviations						
Bond lengths (Å)	0.0070	0.0067	0.0080	0.0088	-	-
Bond angles (°)	1.26	1.24	1.27	1.29		
Validation						
MolProbity score	1.68	1.56	1.48	1.53	-	-
EMRinger score	2.24	3.16	4.06	3.74		
Clashscore	5.87	5.53	4.87	4.94		
Poor rotamers (%)	0.10	0.07	0.10	0.12		
C-beta deviations	0	0	0	0		
CaBLAM outliers (%)	2.14	.2.04	1.75	1.69		
Ramachandran plot						
Favored (%)	94.84	96.12	96.50	96.00	-	-
Allowed (%)	5.15	3.88	3.50	4.00		
Disallowed (%)	0.01	0.00	0.00	0.00		

Table S5

Model and data collection statistics for turnover complex I dataset

	Turnover CxI – closed (EMD-11244) (PDB 6ZKC)	Turnover CxI – open1 (EMD-11245) (PDB 6ZKD)	Turnover CxI – open2 (EMD-11246) (PDB 6ZKE)	Turnover CxI – open3 (EMD-11247) (PDB 6ZKF)	PA-focused refinement (EMD-11241) (PDB 6ZK9)	Open MD-focused refinement (EMD-11242) (PDB 6ZKA)	Closed MD-focused refinement (EMD-11243) (PDB 6ZKB)
Data collection and processing							
Microscope	Titan Krios	Titan Krios	Titan Krios	Titan Krios	Titan Krios	Titan Krios	Titan Krios
Camera	Falcon 3 linear	Falcon 3 linear	Falcon 3 linear	Falcon 3 linear	Falcon 3 linear	Falcon 3 linear	Falcon 3 linear
Magnification	130000x	130000x	130000x	130000x	130000x	130000x	130000x
Voltage (kV)	300	300	300	300	300	300	300
Electron exposure (e–/Å^2)	89	89	89	89	89	89	89
Automation software	EPU	EPU	EPU	EPU	EPU	EPU	EPU
Number of frames	40	40	40	40	40	40	40
Defocus range (μm)	~ -1 to -2	~ -1 to -2	~ -1 to -2	~ -1 to -2	~ -1 to -2	~ -1 to -2	~ -1 to -2
Pixel size (Å)	1.061	1.061	1.061	1.061	1.061	1.061	1.061
Symmetry imposed	C1	C1	C1	C1	C1	C1	C1
Number of micrographs	4239	4239	4239	4239	4239	4239	4239
Initial particle images	344541	344541	344541	344541	344541	344541	344541
Final particle images	15769	81780	98436	48396	315484	315484	29057
Map resolution (Å) at 0.143 FSC threshold	3.1	2.7	2.6	2.8	2.3	2.5	2.9
Refinement							
Initial model used (PDB code)	5LNK	5LNK	5LNK	5LNK	5LNK	5LNK	5LNK
Refinement package	Phenix, real space	Phenix, real space	Phenix, real space	Phenix, real space	Phenix, real space	Phenix, real space	Phenix, real space
Model resolution (Å) at 0.5 FSC threshold	3.3	2.9	2.8	3.0	2.3	2.4	3.0
Local resolution range (Å)	2.6-4.8	2.4-4.8	2.4-4.8	2.4-4.8	2.2-3.0	2.4-3.2	2.6-4.8
Cross-correlation							
Mask	0.825	0.869	0.877	0.860	0.922	0.906	0.859
Volume	0.816	0.859	0.866	0.844	0.913	0.889	0.853
Map sharpening *B* factor (Å^2)	-50	-41	-39	-48	-38	-50	-50
Model composition							
Non-hydrogen atoms	67967	67450	67450	67440	29587	40814	39938
Protein residues	66140	65574	65574	65564	27640	38066	38132
Ligands	1827	1876	1876	1876	475	1455	1360
Waters					1472	1293	446
B factors (Å^2)							
Protein	75	64	60	57	66	53	102
Ligand	102	88	86	82	83	79	124
Waters					55	42	81
R.m.s. deviations							
Bond lengths (Å)	0.0077	0.0082	0.0083	0.0081	0.0085	0.0086	0.0079
Bond angles (°)	1.26	1.26	1.26	1.26	1.27	1.27	1.25
Validation							
MolProbity score	1.59	1.50	1.48	1.50	1.47	1.32	1.48
EMRinger score	3.88	4.54	4.65	4.28	6.57	6.09	4.96
Clashscore	5.46	5.28	4.97	5.11	5.11	4.41	4.92
Poor rotamers (%)	0.10	0.06	0.07	0.06	0.07	0.07	0.06
C-beta deviations	0	0	0	0	0	0	0
CaBLAM outliers (%)	1.79	1.71	1.74	1.66	1.77	1.21	1.59
Ramachandran plot							
Favored (%)	95.80	96.60	96.59	96.55	96.79	97.49	96.55
Allowed (%)	4.19	3.40	3.40	3.44	3.18	2.51	3.43
Disallowed (%)	0.01	0.00	0.01	0.01	0.03	0	0.02

Table S6

Model overview* and comparison with the previous ovine complex I model (5LNK)
*Closed-turnover, unless otherwise stated

	Subunit name	Chain	Range built / (out of total) residues	Un-modelled residues	% atomic model NEW	% atomic model in 5LNK	Cofactors	Notes
CORE	51 kDa	1	9-438 / 445	1-8, 439-445	95.6	97.1	FMN N3(4Fe) NADH	
	24 kDa	2	5-217 / 217	1-4	98.2	98.6	N1a (2Fe)	
	75 kDa	3	6-693 / 704	1-5, 694-704	97.7	97.7	N1b(2Fe) N4 (4Fe) N5 (4Fe)	
	49 kDa	4	1-430 / 430	0	100	90.0	DQ, also rotenone	several conformations; dimethylated Arg85
	30 kDa	5	7-214 / 228	1-6, 215-228	91.2	91.2		
	PSST	6	24-179 / 179	1-23	87.2	86.6	N2 (4Fe)	several conformations
	TYKY	9	1-176 / 176	0	100	100	N6a (4Fe) N6b (4Fe)	
	ND3	A	1-115 / 115	0	100	100		15-50 re-modelled
	ND1	H	1-318 / 318	0	100	100	DQ, also rotenone	several conformations, parts re-modelled
	ND6	J	1-175 / 175	0	100	73.7		
	ND4L	K	1-98 / 98	0	100	87.8		N-formyl Met
	ND2	N	1-347 / 347	0	100	100		
	ND4	M	1-459 / 459	0	100	100	rotenone	N-formyl Met
	ND5	L	1-606 / 606	0	100	84.0		N-formyl Met
SUPERNUMERARY	10 kDa	a	32-75 / 75	1-31	58.7	54.7		
	13 kDa	b	1-95 / 96	96	99.0	99.0	Zn^{2+}	
	18 kDa	c	8-133 / 133	1-7	94.7	92.5		
	39 kDa	d	1-340 / 345	341-345	98.6	87.0	NADPH	previously missing C-terminus and two internal loops
	B8	e	13-98 / 98	1-12	87.8	85.7		
	B13	f	3-115 / 115	1-2	98.3	97.4		
	B14	g	14-127 / 127	1-13	89.8	89.8		
	B14.5a	h	1-112 / 112	0	100	84.8		N-acetyl Ala
	B17.2	i	1-145 / 145	0	100	99.3		
	SDAP-α	j	5-84 / 88	1-4, 85-88	90.9	96.6	Phospho-pantetheine	
	42 kDa	k	1-320 / 320	0	100	70.9		
	15 kDa	l	1-105 / 105	0	100	90.5		
	B9	m	4-83 / 83	1-3	96.4	96.4		
	B12	n	11-89 / 97	1-10, 90-97	81.4	73.2		
	B14.5b	o	1-120 / 120	0	100	100		
	B15	p	1-128 / 128	0	100	62.5		
	B16.6	q	5-143 / 143	1-4	97.2	97.9		
	B17	r	1-38, 66-126 / 127	37-65, 127	76.4	66.1		
	B18	s	1-122 / 136	123-136	89.7	78.7		N- myristoyl Gly
	B22	t	1-177 / 178	178	99.4	93.3		
	AGGG	u	5-69 / 72	1-4, 70-72	90.3	91.7		
	ASHI	v	4-158 / 158	1-3	98.1	27.2		
	ESSS	w	6-123 / 125	1-5, 124-125	94.4	68.8		
	KFYI	x	1-49 / 49	0	100	98.0		
	MNLL	y	8-57 / 57	1-7	87.7	93.0		
	MWFE	z	1-70 / 70	0	100	98.6		
	B14.7	V	1-140 / 140	0	100	0		previously polyAla; N-acetyl Ala
	SGDH	W	5-143 / 143	1-4	97.2	97.2		
	SDAP-β	X	2-88 / 88	1	98.9	100	Phospho-pantetheine	
	PGIV	Y	1-171 / 171	0	100	100		
	PDSW	Z	3-173 / 175	1-2, 174-175	97.7	97.7		
	TOTAL		**8256 / 8516**	**260**	**96.9 %**	**88.3%**		

Table S7

Charge distribution in membrane arm of closed and open complex I during turnover

	ND5 (chain L)						**ND4 (chain M)**				**ND2 (chain N)**				**ND4L (chain K)**		**ND3 (chain A)**	**ND1 (chain H)**	
	K392	K336	H248	K223	D179	E145	E378	K237	K206	E123	K263	K135	K105	E34	E70	E34	D66	E143	E192
Open state				**+** HB to bb O of W144	**0?**	**-** SB to SC of R176	**0** side-chain dens-ity		**0**	**0**	**0** Fewer waters		**+** More waters	**-**	**0**	**0**	**0**	**0**	**0**
Closed state				**0** Fewer waters	**-** SB to SC of R176	**0**			**+** HB to bb O of F122	**-** HB to SC of S157	**+** Stronger side-chain density		**0**	**0**	**-**	**-**	**0**	**-**	**0**

Densities of the key residues, as well as their hydrogen bonds, salt bridges and the number of coordinated waters were compared between the two states.

Lys: + protonated, 0 neutral
Glu: 0 neutral, - deprotonated
SB – salt bridge density, HB – hydrogen bond density.
SC – side chain, bb – backbone.
Empty cell – no clear information.

Movie S1

Opening and closing of complex I result in large scale reorganization of ND1 and ND6 subunits.

Movie S2

Quinone diffusion out of the cavity is aided by conformational changes of the 49 kDa, ND1 and PSST loops during opening and reduction of the complex.

References and Notes

1. L. A. Sazanov, A giant molecular proton pump: Structure and mechanism of respiratory complex I. *Nat. Rev. Mol. Cell Biol.* **16**, 375–388 (2015). doi:10.1038/nrm3997 Medline

2. J. Hirst, Mitochondrial complex I. *Annu. Rev. Biochem.* **82**, 551–575 (2013). doi:10.1146/annurev-biochem-070511-103700 Medline

3. D. A. Stroud, E. E. Surgenor, L. E. Formosa, B. Reljic, A. E. Frazier, M. G. Dibley, L. D. Osellame, T. Stait, T. H. Beilharz, D. R. Thorburn, A. Salim, M. T. Ryan, Accessory subunits are integral for assembly and function of human mitochondrial complex I. *Nature* **538**, 123–126 (2016). doi:10.1038/nature19754 Medline

4. R. Baradaran, J. M. Berrisford, G. S. Minhas, L. A. Sazanov, Crystal structure of the entire respiratory complex I. *Nature* **494**, 443–448 (2013). doi:10.1038/nature11871 Medline

5. R. G. Efremov, L. A. Sazanov, Structure of the membrane domain of respiratory complex I. *Nature* **476**, 414–420 (2011). doi:10.1038/nature10330 Medline

6. K. Fiedorczuk, J. A. Letts, G. Degliesposti, K. Kaszuba, M. Skehel, L. A. Sazanov, Atomic structure of the entire mammalian mitochondrial complex I. *Nature* **538**, 406–410 (2016). doi:10.1038/nature19794 Medline

7. J. Zhu, K. R. Vinothkumar, J. Hirst, Structure of mammalian respiratory complex I. *Nature* **536**, 354–358 (2016). doi:10.1038/nature19095 Medline

8. A. A. Agip, J. N. Blaza, H. R. Bridges, C. Viscomi, S. Rawson, S. P. Muench, J. Hirst, Cryo-EM structures of complex I from mouse heart mitochondria in two biochemically defined states. *Nat. Struct. Mol. Biol.* **25**, 548–556 (2018). doi:10.1038/s41594-018-0073-1 Medline

9. J. A. Letts, K. Fiedorczuk, G. Degliesposti, M. Skehel, L. A. Sazanov, Structures of respiratory supercomplex I+III_2 reveal functional and conformational crosstalk. *Mol. Cell* **75**, 1131–1146.e6 (2019). doi:10.1016/j.molcel.2019.07.022 Medline

10. L. Euro, D. A. Bloch, M. Wikström, M. I. Verkhovsky, M. Verkhovskaya, Electrostatic interactions between FeS clusters in NADH:ubiquinone oxidoreductase (complex I) from *Escherichia coli*. *Biochemistry* **47**, 3185–3193 (2008). doi:10.1021/bi702063t Medline

11. M. Wikström, V. Sharma, V. R. I. Kaila, J. P. Hosler, G. Hummer, New perspectives on proton pumping in cellular respiration. *Chem. Rev.* **115**, 2196–2221 (2015). doi:10.1021/cr500448t Medline

12. V. Sharma, G. Belevich, A. P. Gamiz-Hernandez, T. Róg, I. Vattulainen, M. L. Verkhovskaya, M. Wikström, G. Hummer, V. R. I. Kaila, Redox-induced activation of the proton pump in the respiratory complex I. *Proc. Natl. Acad. Sci. U.S.A.* **112**, 11571–11576 (2015). doi:10.1073/pnas.1503761112 Medline

13. J. Warnau, V. Sharma, A. P. Gamiz-Hernandez, A. Di Luca, O. Haapanen, I. Vattulainen, M. Wikström, G. Hummer, V. R. I. Kaila, Redox-coupled quinone dynamics in the respiratory complex I. *Proc. Natl. Acad. Sci. U.S.A.* **115**, E8413–E8420 (2018). doi:10.1073/pnas.1805468115 Medline

14. O. Haapanen, A. Djurabekova, V. Sharma, Role of second quinone binding site in proton pumping by respiratory complex I. *Front Chem.* **7**, 221 (2019).

doi:10.3389/fchem.2019.00221 Medline

15. M. Verkhovskaya, D. A. Bloch, Energy-converting respiratory complex I: On the way to the molecular mechanism of the proton pump. *Int. J. Biochem. Cell Biol.* **45**, 491–511 (2013). doi:10.1016/j.biocel.2012.08.024 Medline

16. V. R. I. Kaila, Long-range proton-coupled electron transfer in biological energy conversion: Towards mechanistic understanding of respiratory complex I. *J. R. Soc. Interface* **15**, 20170916 (2018). doi:10.1098/rsif.2017.0916 Medline

17. A. Di Luca, A. P. Gamiz-Hernandez, V. R. I. Kaila, Symmetry-related proton transfer pathways in respiratory complex I. *Proc. Natl. Acad. Sci. U.S.A.* **114**, E6314–E6321 (2017). doi:10.1073/pnas.1706278114 Medline

18. J. N. Blaza, K. R. Vinothkumar, J. Hirst, Structure of the deactive state of mammalian respiratory complex I. *Structure* **26**, 312–319.e3 (2018). doi:10.1016/j.str.2017.12.014 Medline

19. S. Matsuzaki, K. M. Humphries, Selective inhibition of deactivated mitochondrial complex I by biguanides. *Biochemistry* **54**, 2011–2021 (2015). doi:10.1021/bi501473h Medline

20. J. A. Letts, G. Degliesposti, K. Fiedorczuk, M. Skehel, L. A. Sazanov, Purification of ovine respiratory complex I results in a highly active and stable preparation. *J. Biol. Chem.* **291**, 24657–24675 (2016). doi:10.1074/jbc.M116.735142 Medline

21. M. H. Olsson, C. R. Søndergaard, M. Rostkowski, J. H. Jensen, PROPKA3: Consistent treatment of internal and surface residues in empirical pK_a predictions. *J. Chem. Theory Comput.* **7**, 525–537 (2011). doi:10.1021/ct100578z Medline

22. E. Galemou Yoga, O. Haapanen, I. Wittig, K. Siegmund, V. Sharma, V. Zickermann, Mutations in a conserved loop in the PSST subunit of respiratory complex I affect ubiquinone binding and dynamics. *Biochim. Biophys. Acta* **1860**, 573–581 (2019). doi:10.1016/j.bbabio.2019.06.006 Medline

23. V. G. Grivennikova, E. O. Maklashina, E. V. Gavrikova, A. D. Vinogradov, Interaction of the mitochondrial NADH-ubiquinone reductase with rotenone as related to the enzyme active/inactive transition. *Biochim. Biophys. Acta* **1319**, 223–232 (1997). doi:10.1016/S0005-2728(96)00163-6 Medline

24. O. Haapanen, V. Sharma, A modeling and simulation perspective on the mechanism and function of respiratory complex I. *Biochim. Biophys. Acta* **1859**, 510–523 (2018). doi:10.1016/j.bbabio.2018.04.001 Medline

25. P. G. Roberts, J. Hirst, The deactive form of respiratory complex I from mammalian mitochondria is a Na^+/H^+ antiporter. *J. Biol. Chem.* **287**, 34743–34751 (2012). doi:10.1074/jbc.M112.384560 Medline

26. V. Zickermann, C. Wirth, H. Nasiri, K. Siegmund, H. Schwalbe, C. Hunte, U. Brandt, Structural biology. Mechanistic insight from the crystal structure of mitochondrial complex I. *Science* **347**, 44–49 (2015). doi:10.1126/science.1259859 Medline

27. A. B. Kotlyar, A. D. Vinogradov, Slow active/inactive transition of the mitochondrial NADH-ubiquinone reductase. *Biochim. Biophys. Acta* **1019**, 151–158 (1990). doi:10.1016/0005-2728(90)90137-S Medline

28. K. Parey, O. Haapanen, V. Sharma, H. Köfeler, T. Züllig, S. Prinz, K. Siegmund, I. Wittig, D. J. Mills, J. Vonck, W. Kühlbrandt, V. Zickermann, High-resolution cryo-

EM structures of respiratory complex I: Mechanism, assembly, and disease. *Sci. Adv.* **5**, eaax9484 (2019). doi:10.1126/sciadv.aax9484 Medline

29. K. Parey, U. Brandt, H. Xie, D. J. Mills, K. Siegmund, J. Vonck, W. Kühlbrandt, V. Zickermann, Cryo-EM structure of respiratory complex I at work. *eLife* **7**, e39213 (2018). doi:10.7554/eLife.39213 Medline

30. A. D. Vinogradov, V. G. Grivennikova, The mitochondrial complex I: Progress in understanding of catalytic properties. *IUBMB Life* **52**, 129–134 (2001). doi:10.1080/15216540152845920 Medline

31. J. Wang, On the appearance of carboxylates in electrostatic potential maps. *Protein Sci.* **26**, 396–402 (2017). doi:10.1002/pro.3093 Medline

32. T. Hayashi, A. A. Stuchebrukhov, Quantum electron tunneling in respiratory complex I. *J. Phys. Chem. B* **115**, 5354–5364 (2011). doi:10.1021/jp109410j Medline

33. M. Schorb, I. Haberbosch, W. J. H. Hagen, Y. Schwab, D. N. Mastronarde, Software tools for automated transmission electron microscopy. *Nat. Methods* **16**, 471–477 (2019). doi:10.1038/s41592-019-0396-9 Medline

34. J. Zivanov, T. Nakane, B. O. Forsberg, D. Kimanius, W. J. Hagen, E. Lindahl, S. H. Scheres, New tools for automated high-resolution cryo-EM structure determination in RELION-3. *eLife* **7**, e42166 (2018). doi:10.7554/eLife.42166 Medline

35. S. Q. Zheng, E. Palovcak, J.-P. Armache, K. A. Verba, Y. Cheng, D. A. Agard, MotionCor2: Anisotropic correction of beam-induced motion for improved cryo-electron microscopy. *Nat. Methods* **14**, 331–332 (2017). doi:10.1038/nmeth.4193 Medline

36. A. Rohou, N. Grigorieff, CTFFIND4: Fast and accurate defocus estimation from electron micrographs. *J. Struct. Biol.* **192**, 216–221 (2015). doi:10.1016/j.jsb.2015.08.008 Medline

37. J. Carroll, I. M. Fearnley, J. E. Walker, Definition of the mitochondrial proteome by measurement of molecular masses of membrane proteins. *Proc. Natl. Acad. Sci. U.S.A.* **103**, 16170–16175 (2006). doi:10.1073/pnas.0607719103 Medline

38. P. Emsley, B. Lohkamp, W. G. Scott, K. Cowtan, Features and development of Coot. *Acta Crystallogr. Sect. D Biol. Crystallogr.* **66**, 486–501 (2010). doi:10.1107/S0907444910007493 Medline

39. P. D. Adams, P. V. Afonine, G. Bunkóczi, V. B. Chen, I. W. Davis, N. Echols, J. J. Headd, L.-W. Hung, G. J. Kapral, R. W. Grosse-Kunstleve, A. J. McCoy, N. W. Moriarty, R. Oeffner, R. J. Read, D. C. Richardson, J. S. Richardson, T. C. Terwilliger, P. H. Zwart, *PHENIX*: A comprehensive Python-based system for macromolecular structure solution. *Acta Crystallogr. Sect. D Biol. Crystallogr.* **66**, 213–221 (2010). doi:10.1107/S0907444909052925 Medline

40. B. A. Barad, N. Echols, R. Y. R. Wang, Y. Cheng, F. DiMaio, P. D. Adams, J. S. Fraser, EMRinger: Side chain-directed model and map validation for 3D cryo-electron microscopy. *Nat. Methods* **12**, 943–946 (2015). doi:10.1038/nmeth.3541 Medline

41. V. B. Chen, W. B. Arendall III, J. J. Headd, D. A. Keedy, R. M. Immormino, G. J. Kapral, L. W. Murray, J. S. Richardson, D. C. Richardson, MolProbity: All-atom structure validation for macromolecular crystallography. *Acta Crystallogr. D Biol. Crystallogr.* **66**, 12–21 (2010). doi:10.1107/S0907444909042073 Medline

42. H. Zheng, M. Chruszcz, P. Lasota, L. Lebioda, W. Minor, Data mining of metal ion environments present in protein structures. *J. Inorg. Biochem.* **102**, 1765–1776 (2008). doi:10.1016/j.jinorgbio.2008.05.006 Medline

43. J. M. Berrisford, L. A. Sazanov, Structural basis for the mechanism of respiratory complex I. *J. Biol. Chem.* **284**, 29773–29783 (2009). doi:10.1074/jbc.M109.032144 Medline

44. M. Schulte, K. Frick, E. Gnandt, S. Jurkovic, S. Burschel, R. Labatzke, K. Aierstock, D. Fiegen, D. Wohlwend, S. Gerhardt, O. Einsle, T. Friedrich, A mechanism to prevent production of reactive oxygen species by *Escherichia coli* respiratory complex I. *Nat. Commun.* **10**, 2551 (2019). doi:10.1038/s41467-019-10429-0 Medline

45. M. Murai, H. Miyoshi, Current topics on inhibitors of respiratory complex I. *Biochim. Biophys. Acta* **1857**, 884–891 (2016). doi:10.1016/j.bbabio.2015.11.009 Medline

46. F. G. P. Earley, S. D. Patel, I. Ragan, G. Attardi, Photolabelling of a mitochondrially encoded subunit of NADH dehydrogenase with [^{3}H]dihydrorotenone. *FEBS Lett.* **219**, 108–112 (1987). doi:10.1016/0014-5793(87)81200-0 Medline

47. S. Uno, T. Masuya, K. Shinzawa-Itoh, J. Lasham, O. Haapanen, T. Shiba, D. K. Inaoka, V. Sharma, M. Murai, H. Miyoshi, Oversized ubiquinones as molecular probes for structural dynamics of the ubiquinone reaction site in mitochondrial respiratory complex I. *J. Biol. Chem.* **295**, 2449–2463 (2020). doi:10.1074/jbc.RA119.012347 Medline

48. A. Galkin, B. Meyer, I. Wittig, M. Karas, H. Schägger, A. Vinogradov, U. Brandt, Identification of the mitochondrial ND3 subunit as a structural component involved in the active/deactive enzyme transition of respiratory complex I. *J. Biol. Chem.* **283**, 20907–20913 (2008). doi:10.1074/jbc.M803190200 Medline

49. O. Haapanen, V. Sharma, Role of water and protein dynamics in proton pumping by respiratory complex I. *Sci. Rep.* **7**, 7747 (2017). doi:10.1038/s41598-017-07930-1 Medline

50. V. R. I. Kaila, M. Wikström, G. Hummer, Electrostatics, hydration, and proton transfer dynamics in the membrane domain of respiratory complex I. *Proc. Natl. Acad. Sci. U.S.A.* **111**, 6988–6993 (2014). doi:10.1073/pnas.1319156111 Medline

51. X. C. Zhang, B. Li, Towards understanding the mechanisms of proton pumps in complex-I of the respiratory chain. *Biophys. Rep.* **5**, 219–234 (2019). doi:10.1007/s41048-019-00094-7

52. M. Sato, P. K. Sinha, J. Torres-Bacete, A. Matsuno-Yagi, T. Yagi, Energy transducing roles of antiporter-like subunits in *Escherichia coli* NDH-1 with main focus on subunit NuoN (ND2). *J. Biol. Chem.* **288**, 24705–24716 (2013). doi:10.1074/jbc.M113.482968 Medline

53. E. Nakamaru-Ogiso, M. C. Kao, H. Chen, S. C. Sinha, T. Yagi, T. Ohnishi, The membrane subunit NuoL(ND5) is involved in the indirect proton pumping mechanism of Escherichia coli complex I. *J. Biol. Chem.* **285**, 39070–39078 (2010). doi:10.1074/jbc.M110.157826 Medline

54. S. Dröse, S. Krack, L. Sokolova, K. Zwicker, H. D. Barth, N. Morgner, H. Heide, M. Steger, E. Nübel, V. Zickermann, S. Kerscher, B. Brutschy, M. Radermacher, U. Brandt, Functional dissection of the proton pumping modules of mitochondrial complex I. *PLOS Biol.* **9**, e1001128 (2011). doi:10.1371/journal.pbio.1001128

Medline

55. G. Belevich, J. Knuuti, M. I. Verkhovsky, M. Wikström, M. Verkhovskaya, Probing the mechanistic role of the long α-helix in subunit L of respiratory complex I from *Escherichia coli* by site-directed mutagenesis. *Mol. Microbiol.* **82**, 1086–1095 (2011). doi:10.1111/j.1365-2958.2011.07883.x Medline

56. S. Steimle, C. Bajzath, K. Dörner, M. Schulte, V. Bothe, T. Friedrich, Role of subunit NuoL for proton translocation by respiratory complex I. *Biochemistry* **50**, 3386–3393 (2011). doi:10.1021/bi200264q Medline

57. P. J. Holt, D. J. Morgan, L. A. Sazanov, The location of NuoL and NuoM subunits in the membrane domain of the *Escherichia coli* complex I: Implications for the mechanism of proton pumping. *J. Biol. Chem.* **278**, 43114–43120 (2003). doi:10.1074/jbc.M308247200 Medline

58. N. Battchikova, M. Eisenhut, E. M. Aro, Cyanobacterial NDH-1 complexes: Novel insights and remaining puzzles. *Biochim. Biophys. Acta* **1807**, 935–944 (2011). doi:10.1016/j.bbabio.2010.10.017 Medline

59. J. M. Schuller, P. Saura, J. Thiemann, S. K. Schuller, A. P. Gamiz-Hernandez, G. Kurisu, M. M. Nowaczyk, V. R. I. Kaila, Redox-coupled proton pumping drives carbon concentration in the photosynthetic complex I. *Nat. Commun.* **11**, 494 (2020). doi:10.1038/s41467-020-14347-4 Medline

60. M. E. Mühlbauer, P. Saura, F. Nuber, A. Di Luca, T. Friedrich, V. R. I. Kaila, Water-gated proton transfer dynamics in respiratory complex I. *J. Am. Chem. Soc.* **142**, 13718–13728 (2020). doi:10.1021/jacs.0c02789 Medline